Research article

Claudin-10b cation channels in tight junction strands: Octameric-interlocked pore barrels constitute paracellular channels with low water permeability

Santhosh Kumar Nagarajan, Stanislav Klein, Bita Sokhandan Fadakar, Jörg Piontek *

Clinical Physiology/Nutritional Medicine, Department of Gastroenterology, Rheumatology and Infectious Diseases, Charité–Universitätsmedizin Berlin, Hindenburgdamm 30, 12203 Berlin, Germany

ARTICLE INFO

ABSTRACT

Claudin proteins constitute the backbone of tight junctions (TJs) regulating paracellular permeability for solutes and water. The molecular mechanism of claudin polymerization and paracellular channel formation is unclear. However, a joined double-rows architecture of claudin strands has been supported by experimental and modeling data. Here, we compared two variants of this architectural model for the related but functionally distinct cation channel-forming claudin-10b and claudin-15: *tetrameric-locked-barrel* vs *octameric-interlocked-barrels* model. Homology modeling and molecular dynamics simulations of double-membrane embedded dodecamers indicate that claudin-10b and claudin-15 share the same joined double-rows architecture of TJ-strands. For both, the results indicate *octameric-interlocked-barrels*: Sidewise unsealed tetrameric pore scaffolds interlocked with adjacent pores via the β1β2 loop of the extracellular segment (ECS) 1. This loop mediates hydrophobic clustering and, together with ECS2, *cis*- and *trans*-interaction between claudins of the adjacent tetrameric pore scaffolds. In addition, the β1β2 loop contributes to lining of the ion conduction pathway. The charge-distribution along the pore differs between claudin-10b and claudin-15 and is suggested to be a key determinant for the cation- and water permeabilities that differ between the two claudins. In the claudin-10b simulations, similar as for claudin-15, the conserved D56 in the pore center is the main cation interaction site. In contrast to claudin-15 channels, the claudin-10b-specific D36, K64 and E153 are suggested to cause jamming of cations that prevents efficient water passage. In sum, we provide novel mechanistic information about polymerization of classic claudins, formation of embedded channels and thus regulation of paracellular transport across epithelia.

1. Introduction

Tight junctions (TJs) regulate paracellular permeability in epithelia and endothelia in a size- and charge-selective manner. These cell-cell junctions are defined by apparent fusion points of opposing cell membranes and meshworks of intramembranous fibrils (TJ strands), visualized by EM [1–3] and super-resolution light microscopy [4,5]. TJs represent multi-protein complexes including different membrane-associated scaffolding, signaling, and transmembrane proteins (mainly claudins, TAMPs, and JAMs). Most of the latter are attached and regulated by the scaffolding proteins (e.g. ZO-1) contributing to junctional stability and dynamics [6–8].

The claudin (CLDN) tetraspan membrane proteins form the backbone of TJ strands and bridge the paracellular cleft, constituting the barrier and channels that directly regulate paracellular permeation [9,10]. Functionally, the ~27 mammalian family members can be roughly grouped into (i) barrier-forming claudins (such as CLDN1, −3, −5, −11) that block solute permeation nearly completely, (ii) channel-forming claudins (such as CLDN2, −10a, −10b, −15, −17) that form charge- and size-selective channels and (iii) context-dependent claudins (such as CLDN4, −7, −8, −16) with permeability properties that strongly depend also on other TJ components [11]. Based on sequence similarity, claudins can be grouped into classic (typical) and non-classic (atypical) claudins [12], with the former displaying higher sequence homology and proposed to follow a largely similar basic TJ strand assembly mechanism, mediated by common sequence motifs [10,13–15]. Most of the classic claudins can self-assemble into TJ-like strands in cells, whereas strand incorporation of

---

* Corresponding author.
  E-mail address: joerg.piontek@charite.de (J. Piontek).
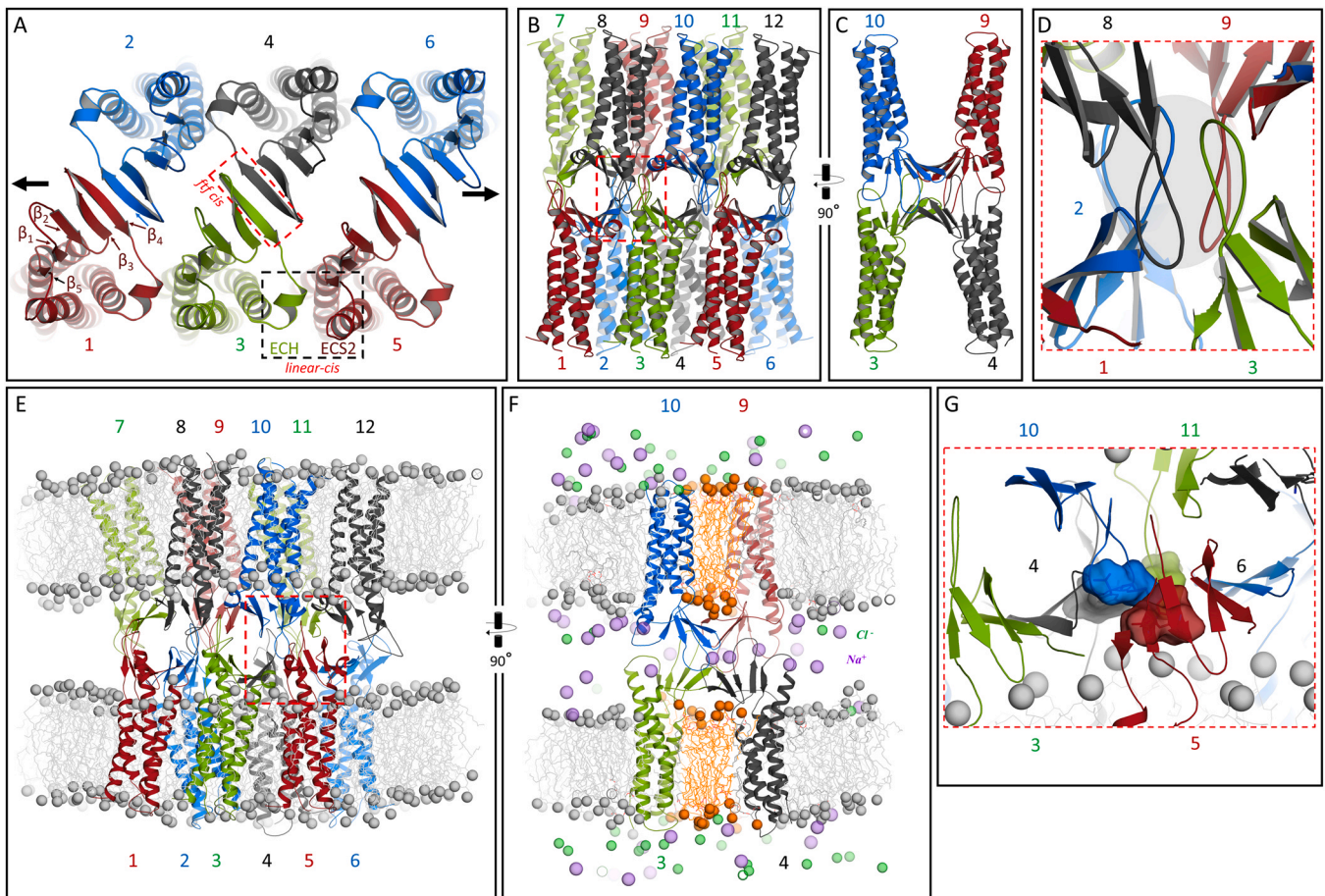
Fig. 1. (A-D) CLDN10b dodecamer starting model: *tetrameric-locked-barrel* model 10b_*4LBS1*. Claudin chains are shown as colored cartoons. **(A)** In one membrane, multiple chains form an anti-parallel double row by linear-cis (black box) and face-to-face(ftf)-*cis* (red box) interfaces. Top view from extracellular side, six chains [1–6] are shown, arrows indicate strand elongation by additional cfhains. β-strands 1–5, extracellular helix region (ECH) and ECS2 are marked. **(B)** Side view on the 12 claudin chains [1–12]. Joined double rows (JDR) architecture comprising extracellular *cis*- and-*trans*-interfaces resulting in β-barrel-like pore scaffold [10,14]. The model contains ECS2-ECS2-*trans* interface (e.g. between chain 3 and 8 in red box) and central *cis/trans* cluster of four ECS1-β1β2 loops suggested by Hempel et al. [15]. **(C)** Turned-view on central *tetrameric-locked barrel* pore. **(D)** Close up (of red box, B) showing central cluster of β1β2 loops of chains 2, 3, 8, 9 (gray oval). **(E-G) 10b_*4LBH2* model after MD simulation**. Snapshot of production run at 100 ns. **(E)** Side view, claudins chains shown as colored cartoon, POPC lipids as lines and phosphates as spheres. In the membrane between the two claudin rows, next to and below the ECS β-sheets, lipids (orange) are trapped. In pore center, only Na$^+$ (magenta spheres) but no Cl$^-$ (green spheres) ions are present, demonstrating expected charge selectivity of the modeled channels (See also Fig. S3 A-H). **(G)** Close up (of red box, E) showing central β1β2 loop cluster. Hydrophobic V39 & I40 at loop tip of chains 10 & 11 (blue, green) and close-by V32 & W46 of chains 4 & 5 (black, red) are shown (surface) as contact example. In average, distances were larger (Fig. 2).

most non-classic claudins depends on co-oligomerization with classic claudins [5,10]. Claudins polymerize by interaction between molecules (chains) within one membrane (*cis*) and two opposing membranes at cell-cell contacts (*trans*) [12]. Hetero-oligomerization is possible for compatible claudins only [5,10,16,17].

The molecular mechanism of claudin oligo/polymerization resulting in strand and channel formation is largely unclear. Different architectural models have been suggested for CLDN15 and other classic claudins [10,14,15,18–23]. The joined double rows (JDR) model of CLDN15 suggested by Suzuki et al. [14], refined [24,25] and expanded to other classic claudins based on sequence homology [15,26], is the one that is supported most by experimental and modeling data [10]. According to this model, claudin chains *cis*-interact in a linear and face-to-face (ftf) manner resulting in an anti-parallel double-row of claudin chains within one membrane. *Trans*-interactions between the claudins join the two double rows of opposing cell membranes into functional strands (Fig. 1A-D). Following this model, it was proposed that claudins assemble into *cis*-oligomer before *trans*-interaction at cell-cell contacts triggers polymerization [15]. However, different Suzuki/JDR model variants have been

suggested by molecular dynamics (MD) simulations [24,25,27,28] and combination of experimental and modeling data [15]. The models differ mainly in orientation of the loop between the β1-and β2-strands (β1β2 loop, part of variable region V1 [29]) of the extracellular segment (ECS) one. Hempel et al. suggested a straight β1β2 loop extension and orientation towards the chains in the opposing membrane (Fig. 1D, [15]). This results in a *tetrameric-locked-barrel* channel conformation (*4LB* model) in which nearly the complete pore is lined only by residues from four chains. Only close to the pore entrance, a few residues from neighboring tetramers contribute to pore-lining. In contrast, Samanta et al. suggested a more kinked/flat β1β2 loop orientation towards a claudin chain in the same membrane [25]. This results in an *octameric-interlocked-barrels* channel conformation (*8IB* model) in which eight chains line the pore in the inner pore region.

Here, we tested and refined Suzuki's JDR strand model by comparing the *4LB*- and *8IB* model variants for CLDN10b and CLDN15 that share high sequence similarity (Fig. S1) and charge selectivity but differ in monovalent cation preference and water permeability. We established a workflow based on homology modeling, distance

constraints, and Desmond MD simulations. The results support an *octameric-interlocked-barrels JDR* model of strands formed by classic claudins such as CLDN10b and -15. In addition, the data indicate that the charge distribution along the pore that differs between CLDN10b and -15 is key for the respective cation and water permeability.

2. Material and methods

2.1. Modeling and simulation platform

The molecular modeling, molecular dynamics and analysis of simulation trajectories were performed using Schrödinger Maestro BioLuminate platform (BioLuminate, version 3.9.079, Release 2020–2, Schrödinger, LLC, New York, NY, 2020), installed in a Linux X86–64 environment. BioLuminate and Schrödinger PyMOL 2.5.2 (http://www.pymol.org/pymol) were used for the visualization of models and image generation. Visual molecular dynamics (VMD) was also used for analysis of simulation trajectories (https://www.ks.uiuc.edu/Research/vmd).

2.2. Homology modeling

Homology models of human CLDN10b (Uniprot P78369–1, 1–186) were created using the advanced homology modeling module of Schrödinger Maestro or PyMod3 [30] (http://schubert.bio.uniroma1.it/pymod), with the CLDN15 crystal structure (PDB ID: 4P79) as template. For the *4LB* variant (see below), the missing β1β2 loop was modeled ab initio [15]. For the *8IB* variant, a β1β2 loop conformation predicted by AlphaFold (https://colab.research.google.com/github/deepmind/alphafold/blob/main/notebooks/AlphaFold.ipynb; [31,32]) was used. In addition, homology models of human CLDN15 (Uniprot P56746, 1–186) were created using chains of CLDN10b_*4LBH* and CLDN10b_*4LBS* starting models as templates. A claudin molecule, the polypeptide chain, is here denoted as chain.

2.3. Generation and MD simulations of CLDN10b and CLDN15 4LB dodecamer models

The initial CLDN10b *4LB* dodecamer model was based on our previously reported CLDN10b octamer model [15,33]. This model was extended into a dodecamer by aligning four chains of octamer duplicates, resulting in a three-pore model formed by two *trans*-interacting hexamers. Based on hypothesis-driven distance constraints based on in vitro data [10,15,33], the dodecamer model was further refined using 'MacroModel Minimization' module present in Schrödinger BioLuminate and a water-solvated environment with gradient convergence threshold of 0.05 kJ mol^{-1} Å^{-1}. As this model consists of a β-barrel like pore formed by the four central chains, it was named as CLDN10b *tetrameric-locked-barrel* Hempel homology model, *10b_4LBH*. In addition, a variation of *4LBH* (named *10b_4LBS*) was modelled directly using 12 chains of the original Suzuki CLDN15 polymer template [14], CLDN10b monomer homology models [15] and less distance constraints than for *4LBH*. For CLDN15, two similar dodecamer variants were modeled using the corresponding CLDN10b variants as templates. Respective CLDN15 homology models were minimized with similar distance constraints as the CLDN10b models and named *15_4LBH* and *15_4LBS*, respectively.

The simulations were carried out using the 'Desmond Molecular Dynamics' module available in BioLuminate (D. E. Shaw Research, New York, NY, 2021. Maestro-Desmond Interoperability Tools, Schrödinger, New York, NY, 2021; [34]). Each model was embedded in a double bilayer membrane system containing 1-palmitoyl-2-oleoyl-sn-glycero-3-phosphocholine (POPC) lipids (~600 in each bilayer). Positioning of proteins in membrane (PPM, [35]) was used to place the protein in the bilayers. POPC molecules were added using the system builder in BioLuminate. Missing lipids that were

not added automatically due to steric hindrance with ECS β-sheets were added manually to avoid water inclusion. The dodecamer with membrane was separated into two hexamer systems with their respective membranes for relaxation (BioLuminate default protocol) and equilibration for 10 ns with force constant of 10 kcal mol^{-1} Å^{-2} applied on protein with NPγT ensemble. Afterwards, hexamers were combined to form a dodecamer with double bilayer system and size of 130:110:150 Å (X:Y:Z axes).

TIP3P waters [36], charge-neutralizing ions and 0.15 M Na$^+$Cl$^-$ were added to the system. The simulations were performed in OPLS3e force field [37] that behaves similar to CHARMM36 force field (e.g. for POPC containing systems [38]), in either NPT or NPγT ensemble, with temperature at 310 K, pressure at 1.01325 bar and for NPγT ensemble, surface tension at 4000 bar× Å. Nosé –Hoover chain method [39] was used as thermostat and Martyna-Tobias-Klein method [40] as barostat. 'Desmond Minimization' of systems was performed for 100 ps and the systems were relaxed using BioLuminate default protocol. Then, the models were equilibrated stepwise by slowly lowering the constraints, starting with constraints on whole protein for 10 ns (10 kcal mol^{-1} Å^{-2}). First side chains, then backbone, stepwise for loops, β-sheets, and helices as well as force constants (5–0 kcal mol^{-1} Å^{-2}) were gradually released over 80 – 130 ns. The individual equilibration steps differed slightly for each model resulting in two simulation variants for each starting model (10b_*4LBH1* and-*2*, 10b_*4LBS1* and-*2*, 15_*4LBH1* and-*2*, 15_*4LBS1* and-*2*). Different simulation conditions that distinguish these models from each other are given in Table S1. After equilibration, the CLDN10b models were simulated for 100 ns and the CLDN15 models for 55–60 ns without any constraints (production run). For all the simulations, reversible reference system propagator algorithms (RESPA) integrator was used to integrate the bonded interactions with a timestep of 2.0 fs.

2.4. Generation and MD simulations of CLDN10b 8IB dodecamer models

For generation of *8IB* dodecamer models, the Suzuki CLDN15 polymer [14] was used as template. After alignment, each chain was exchanged by a CLDN10b homology model containing a β1β2loop conformation that was (compared to those of *4LB* models) kinked/flatter. This resulted in loop overlaps leading to interlocked pore barrels similar as suggested by Samanta et al. for CLDN15 channels [25]. Similar to *4LB* models, this dodecamer model was further refined with a series of minimization steps, using distance constraints to optimize the model based on the following data-derived assumptions (working hypothesis): (i) face-to-face (ftf) interface: C63-C63H-bonds, (ii) linear-*cis* interface: M69 residing inside pocket formed by F146, F147, L158. (iii) β1β2loop conformation: V39/I40 maintain inter-chain contacts, (iv) proximity between T38 and Q154 as indicated by sequence correlation among CLDN10b/15-like sequences in vertebrates, (v) D36 and E153 were oriented towards pore to avoid interference with ECS2-ECS2-*trans* or linear-*cis* interface.

In addition, due to suggested bending capacity of claudin's transmembrane helix 3 (TM3) [41], distance-constrained minimization was used that pulled TM3-ECS2 segment (residues 135 – 147) inwards to avoid clashes of ECS2 segments in *trans*. To increase symmetry, chains of the dimer with best *trans*-interface between two ECS2-β1β2 regions were extended to the other chains of the dodecamer. Different refined variants were checked for their consistency with considerations mentioned above. The best dodecamer was embedded in a double-bilayer POPC membrane. The PPM server was used to orient the protein in the membrane and CHARMM-GUI Membrane builder tool (https://www.charmm-gui.org/) was used to generate the POPC lipids. Missing lipids that were not added automatically due to steric hindrance with ECS β-sheets were added manually to avoid water inclusion. TIP3P water molecules, charge-

neutralizing ions and 0.15 M Na⁺Cl⁻ were added to the system. Similar to the *4LB* models, dodecamer with membrane was separated into two *cis*-hexamers, minimized, relaxed and preequilibrated separately in NPγT ensemble, and then combined for further equilibration (80–130 ns). We followed a series of simulations in the OPLS3e force field with gradually reducing the constraints, similar as for the *4LB* models. The first production run, with M69 and backbones of F146/F147 (linear-*cis* interface) constrained with 1 kcal mol⁻¹ Å⁻², was simulated for 100 ns (*8IBli* model). Afterwards, a second production run without any constraints was simulated for 100 ns (*8Ibno* model). Using one of the early frames from the *8Ibli* model, we modeled two CLDN10b mutants: CLDN10b_K64M and CLDN10b_D36H/A47E/A52S/Y45I/K64W/E153G (CLDN15-like). 'Mutate' panel present in 'Protein Preparation and Refinement' module of BioLuminate was used to create the mutated structures. Similar to *8IB* models, mutant models were embedded in a double membrane, equilibrated, and afterwards production runs, similar to *8Ibli*, were conducted for 100 ns.

2.5. Analysis of the MD trajectories

To analyze potential interactions between residues of different interface chain pairs over time, contact maps were generated. For that an in-house Python3 [42] script was developed and implemented using MDAnalysis (version 2.3.0) [43,44], an object-oriented Python library, to analyze MD simulations. First, topology and trajectory output files from 100 ns MD simulations were loaded through universes in MDAnalysis. Then, for user-defined residue ranges of an interface chain pair, the minimum distance between all atoms of two considered residues was calculated in a so-called contact matrix. These calculations were performed for all chain pairs in a dodecamer model that formed the interface type (e.g., linear-*cis*) of interest. Finally, all contact matrices were used to calculate a mean contact matrix for the considered interface, which was visualized as a heat map, named as the contact map. To represent the potential *cis*- and *trans*-interfaces in the JDR arrangement of strands, mean contact maps were generated for following chain pairs (numbering see Fig. 1) and residue regions: (**a**) linear-*cis*: K64-R80/V32-D36,I142-L158, 8x, chain pairs 1/3, 3/5, 2/4, 4/6, 1/9, 9/11, 8/10, 10/12; (**b**) face-to-face-*cis*: T60-D65; 6x, chain pairs 1/2, 3/4, 5/6, 7/8, 9/10, 11/12; (**c**) crosswise-*cis*: S33-A43_T55-V60/ S33-A43_T55-V60; 4x, chain pairs 2/3, 4/5, 8/9, 10/11; (**d**) K64-*trans*: K64-S68/I35-V39; 4x, chain pairs, 3/10, 10/3, 9/4, 4/9; (**e**) β1β2 loop_ECS2- β1β2 loop_ECS2-*trans*: V32-W46,G145-A160/V32-W46,G145-A160; 4x, chain pairs 2/9, 3/8, 4/11, 5/10; (**f**) β3β4 loop-*trans*: V54-T58/ V54-T58; 4x, chain pairs 2/8, 3/9, 4/10, 5/11; (**g**) β1β2-β3β4 crosswise-*trans*: V32-V60/ V32-V60; 4x, chain pairs 2/8,3/9, 4/10, 5/11.

For analysis and visualization of claudin pore dimensions, another Python3 [42] script was implemented using the 'MDAnalysis.analysis.hole2' module containing the tools to interact with the HOLE program [45,46]. Using the script, the mean pore radius over a user-defined simulation frame range was calculated. Protein secondary structure elements of claudins in MD trajectories were analyzed by using the python library MDTraj [42,47] which allowed for the computation of a dictionary of protein secondary structure assignments (DSSP) [48] for each chain residue for all simulation frames. The program was used to create a secondary structure probability plot for a user-specified residue range averaged over user-defined protein chains and frame range. Solvent-Accessible Surface Area (SASA) values were calculated using VMD (https://www.ks.uiuc.edu/Research/vmd/mailing_list/vmd-l/att-18670/sasa.tcl).

Other model parameters (e.g., H-bonds, candidate residue distances) were analyzed using internal BioLuminate tools, data export and Microsoft Excel.

3. Results

3.1. Generation of tetrameric-locked-barrel dodecamer models (4LB) for CLDN10b and CLDN15

Previously, the *tetrameric-locked-barrel* (*4LB*) model of CLDN10b channels was generated based on experimental support [15] and the CLDN15 strand model [14]. This CLDN10b octamer model was slightly refined [33] and expanded to a dodecamer model, consisting of three adjacent tetrameric pores. This was done to generate a (central) pore that is connected at both sides to a neighboring pore and thus contains all inter-chain interfaces of Suzuki's polymer model [14,25].

This model (CLDN10b *tetrameric-locked-barrel* Hempel homology model, *10b_4LBH*) was based on in vitro data-/hypothesis-driven distance constraints [15,33]. In addition, a second dodecamer model variant (CLDN10b *tetrameric-locked-barrel* Suzuki homology model, *10b_4LBS*. Fig. 1A-D) was generated that contained the same interface types (see below), but less distance constraints and thus was closer to the original Suzuki CLDN15 template. Furthermore, two corresponding dodecamer starting models for CLDN15 were generated using the respective CLDN10b models as template, resulting in *15_4LBH* and *15_4LBS*. These four models were compared using Desmond-based molecular dynamics (MD) simulations.

Each of these four models was embedded in two POPC membranes, NaCl and water were added, and systems were generated. Relaxation and equilibration protocols were established in which constraints were gradually released (see methods). Differences in the equilibration protocols led to two simulation variants for each model (eight simulation lines in total, Table S1, for CLDN10b see also Fig. S2). Afterwards, for each model, MD simulation production runs (CLDN10b: 100 ns, CLDN15: 55–60 ns) without constraints were performed and analyzed to investigate the stability, dynamics, and plausibility of the dodecamer model variants.

As an example, the 100 ns snapshot of the 10b_4LBH2 simulation is shown in Fig. 1E-G. Similar as shown for this model, for all eight simulated models the chains were embedded well in the membrane. Strikingly, in the central region between the two claudins rows of one membrane, lipids are trapped and hardly exchanged with other lipids (Fig. 1F). This suggests a special lipid micro domain around claudins containing not only bulk lipids but also (i) central and (ii) peripheral annular/shell lipids and possibly (iii) non-annular lipids binding stronger to particular sites.

Concerning the protein, the overall arrangement of the starting models (inter-chain interfaces and open β-barrel-like pore) was preserved (Fig. 1). All interface types (linear-*cis*-, face-to-face-*cis*, ECS2-ECS2-*trans* interfaces and central β1β2 loop cluster) were largely maintained. However, individual interfaces (of a particular interface type) varied in detail slightly over time between the different chains and between the four model lines. In the following, the MD simulations of the models were evaluated and compared in detail.

3.2. Evaluation of the CLDN10b tetrameric-locked-barrel dodecamer models

3.2.1. RMSD indicates overall stability of the dodecamer models
To evaluate the oligomer stability during the production run, the root-mean-square-deviation (RMSD) of the protein backbone with respect to the initial structure was calculated for the chains of the central tetramer. The mean RMSD for all four models (*4LBH1*, *4LBH2*, *4LBS1*, *4LBS2*) over the last 50 ns of simulation time was constantly < 2 Å (Fig. S4A), indicating overall stability of the membrane-embedded-oligomers. The secondary structure of the claudin chains was well-preserved in average (Fig. S4B). For all four models, the mean root-mean-square fluctuation (RMSF) of most residue backbones in the central tetramer was < 1.5 Å, further indicating
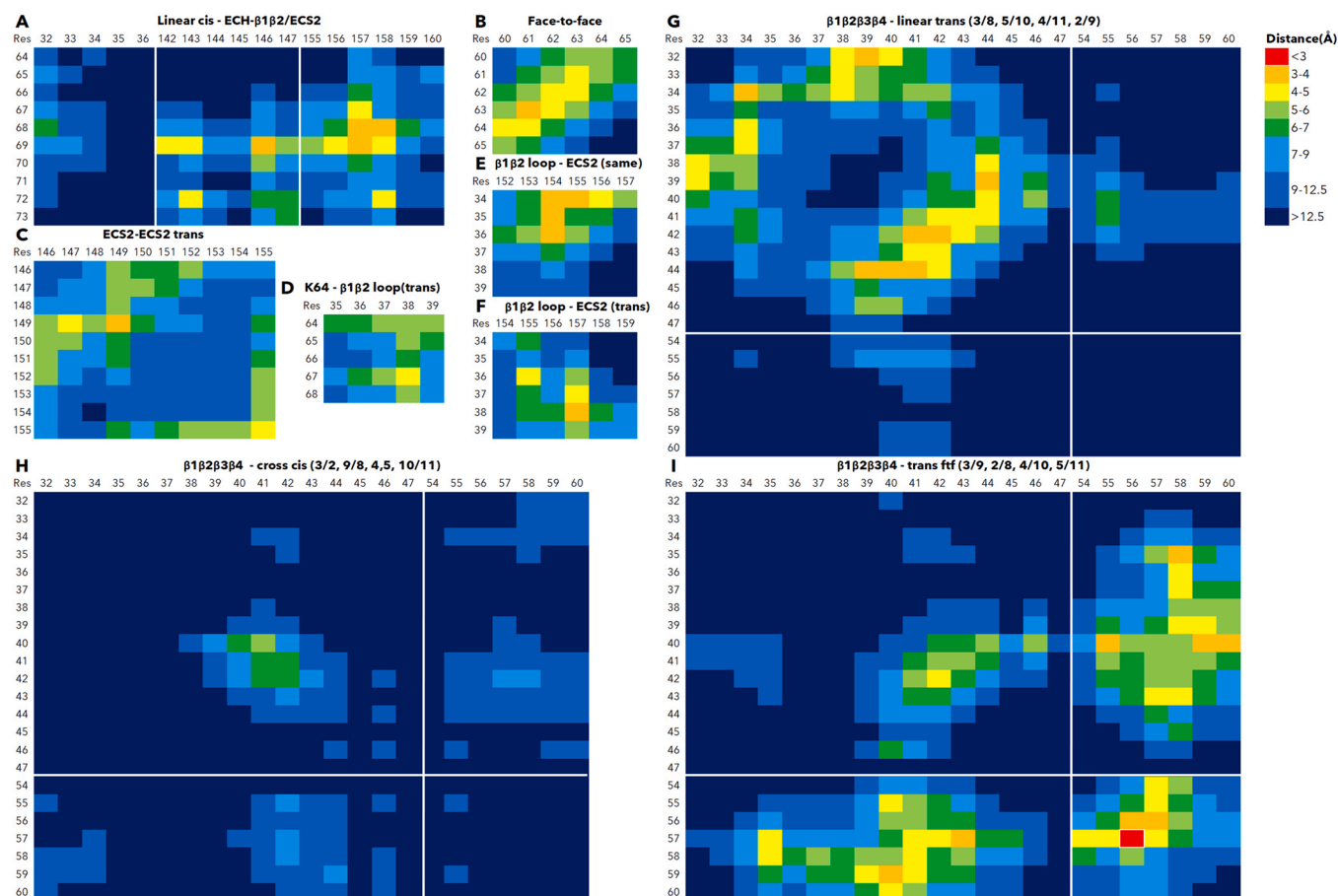
Fig. 2. Inter-chain contact maps for the CLDN10b *tetrameric-locked-barrel* (*4LB*) models. Mean distances (closest atoms) between the numbered residues of protein region pairs reflecting the different interface types. For each interface type, the multiple individual interfaces in one dodecamer and in the four models (*4LBH1*, *4LBH2*, *4LBS1*, *4LBS2*) were averaged. Shown are interaction-relevant parts of contact maps (containing regions with distances < 9 Å and/or parts to be compared) categorized according to interface types. **(A)** Linear-*cis*. **(B)** Face-to-face-*cis*. **(C)** ECS2-ECS2-*trans*. **(D-F)** β1β2 loop with neighboring K64-region and ECS2. **(G-I)** Central cluster of β1β2β3β4 loops, three different chain pairs (numbering see Fig. 1B, D). The contact maps provide interface fingerprints for the CLDN10b *4LB* model.

stability. However, in addition to the intracellular regions, the RMSF was higher for the ECS2 (up to 2.7 Å) and extracellular helix (ECH) region (up to 2.1 Å), indicating higher structural variability of these regions during the simulations.

3.2.2. Defining the dodecamer inter-chain interfaces by residue contact maps

As fingerprints that characterize the interfaces forming the claudin oligomer, inter-chain residue contact maps were created. Contact maps were generated for all pairs of neighboring chains, covering the potential *cis*- and *trans*-interfaces in the joined double-rows (JDR) arrangement of the dodecamer (Fig. 1A-D). The contact map regions of the different chain pairs covering the same interface type (e.g., linear-*cis*) were averaged for each model (model contact maps for *4LBH1*, *4LBH2*, *4LBS1*, *4LBS2*). In addition, mean contacts maps covering all four models were calculated (see methods for details).

For certain residue pairs, the distances differed to a certain extent between the contact maps of different models. This reflects slight differences between the four models. However, for all models the contact maps fitted to the JDR arrangement of claudins within strands [14,15,24]. To provide a compact overview, interaction-relevant regions of the mean contact maps are shown (Fig. 2). For the linear-*cis* interface, closest distances were found for M69 with I142/T143/F146/Y156/E157/L158 and S68 with E157/L158. In addition, proximity between L72 and T143/F146/F147/L158 was detected

(Fig. 2A, linear-*cis* map). For face-to-face-*cis* interface, closest distances were found between the pairs 62/62, 62/63, 63/61, 64/60, 64/61 (Fig. 2B, face-to-face map). In ECS2-ECS2-*trans*, closest distances were detected between P149 and F147/P149 and between two K155 (Fig. 2C, ECS2-ECS2-*trans* map).

The β1β2 loop was part of several chain pair contacts (for definition, see headlines of Fig. 2D-I and chain numbering of Fig. 1B, D):

As suggested earlier [15,33], the β1β2 loop was involved in *trans*-interactions. T38 to T42 of the β1β2 loop were close to V32/T44/W46 at the non-pore-lining side of the ECS-β-sheets of other chains; in addition, T34 and T41-A43 of two loops were very close to each other (Fig. 2G, β1β2β3β4_linear-*trans* map, *trans*-pairs in one claudin row). Also, *cis*-proximity between V39/I40 of two chains was detectable (Fig. 2H, β1β2β3β4_cross-*cis* map, *cis*-crosswise between rows), though with larger mean distance (> 6 Å) than suggested [15]. Proximities between the β3β4 loop and another β3β4 or β1β2 loop are also shown (Fig. 2G-I, β1β2β3β4maps). Here, very close proximity between S57 and V54-S57 and between two D56 of *trans*-pairs between rows were prominent (Fig. 2I,β1β2β3β4_tra*ns*_ftf map). Further contact maps are shown for β1β2 in *trans* with the region around K64, in *trans* with ECS2 and in same chain with ECS2 (Fig. 2D-F). I35 to V39 were close to K64 in *trans*, T38 close to P67 and E157 in *trans* and, within the same chain, T34 was close to Q154-Y156 and I35/D36 close to Q154.

In sum, the contact maps provide detailed interface fingerprints for the *tetrameric-locked-barrel* (*4LB*) CLDN10b model.
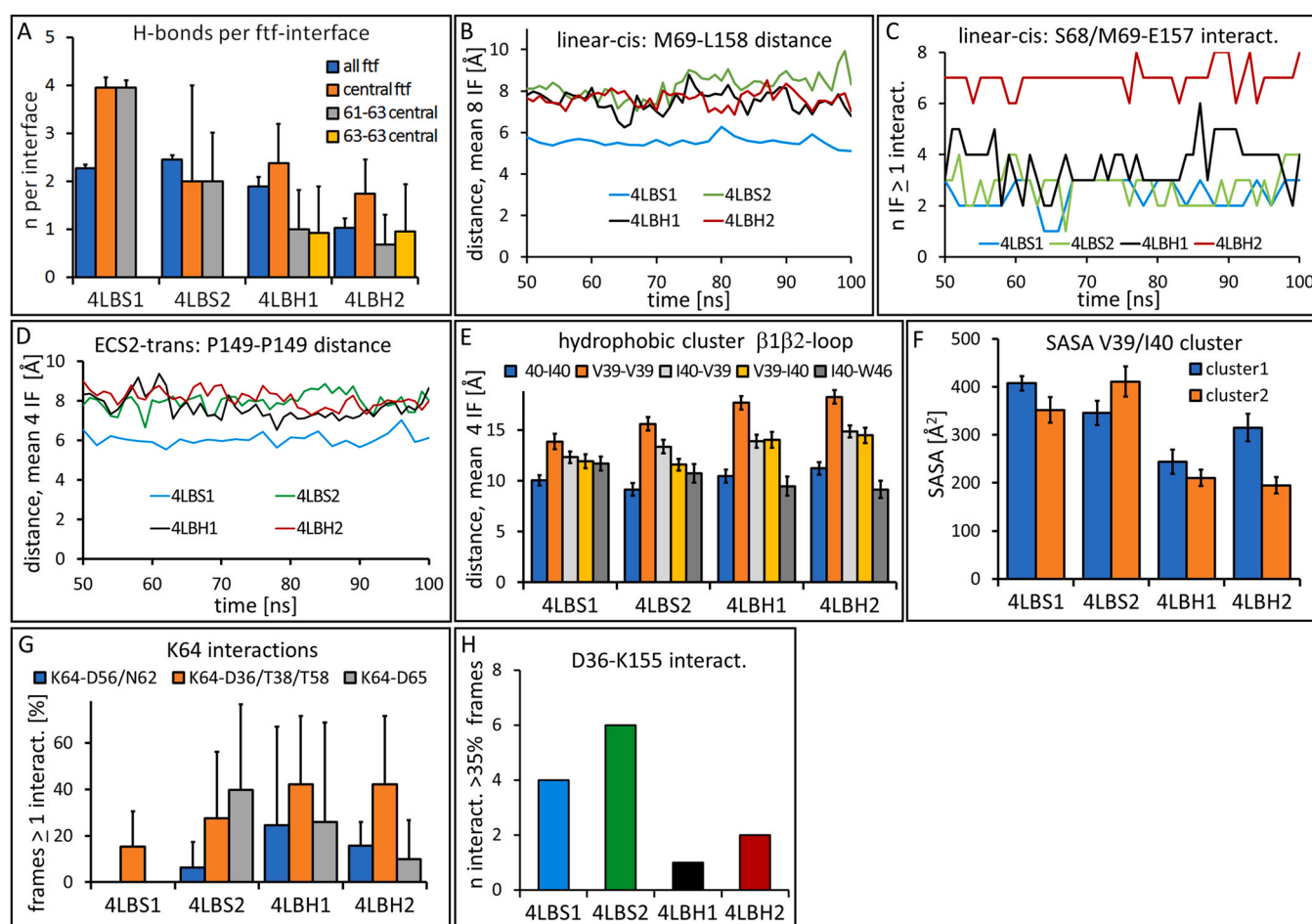
Fig. 3. Detailed interface analysis for CLDN10b *tetrameric-locked-barrel* models *4LBS1*, *4LBS2*, *4LBH1* and *4LBH2*. (**A**) Face-to-face-*cis* (ftf) interface: T58-D65 backbone H-bond counts per interface, for all six (all) and central two (central) interfaces of dodecamer. In addition, counts for 61–63 and 63–63 residue pairs for central interfaces. Mean ± SD. (**B**) Linear-*cis* interface: M69(C_ε)-L158(C_γ) distances over time. Mean of eight interfaces in dodecamer. (**C**) Linear-*cis* interface: number of interfaces (IF, out of eight) with $\geq$ one S68/M69-E157 (side & main chain) electrostatic interaction counts over time. (**D**) ECS2-*trans* interface: P149(C_α)-P149(C_α) distances over time. Mean of four interfaces in dodecamer. (**E**) β1β1β2 loop cluster: pairwise distances for V39-V39, I40-I40, V39-I40, I40-V39 (*cis*, C_β-C_β) and I40-W46 (*trans*, C_β-$C_{\varepsilon2}$). Mean+SD of four (eight for I40-W46) interfaces in dodecamer. (**F**) β1β2 loop cluster: SASA for V39/I40 of four interacting chains, two clusters for each dodecamer model. Mean+SD. (**G**) K64 orientation and interactions: % of frames with $\geq$ one interaction count for NH_3^+ of K64 with following residues (side or main chain): (i) D56/N62 same or other chain, *cis;* (ii) D36/T38, *trans* or T58, *cis*; (iii) D65, same chain. Mean ± SD for four K64 in central tetramer. (**H**) D36 orientation: number of D36-K155 pairs (*trans* or same chain, in total 16 in dodecamer) interacting in > 35% of frames. For (A) the last 20 ns, and (B-H) the last 50 ns of production run were analyzed.

3.2.3. Variability between the CLDN10b tetrameric-locked-barrel models and over simulation time

Next, the different interface types were further evaluated. Differences between the four models (*4LBH1*, *4LBH2*, *4LBS1*, *4LBS2*) and for some interaction types also the variability over the simulation time of the production run was analyzed.

Hallmark of the face-to-face-*cis* interface is the contact between two β4-strands (Fig. 1A, 2 B) strongly mediated by backbone H-bonds [14,15,24,25]. Thus, we counted the H-bonds between the corresponding T58 to D65 residue backbones per interface for the central two and all six chain pairs in the dodecamer (Fig. 3A). Between the models, the H-bond count varied between ~1 and ~2 (regarding all pairs), or ~2 and ~4 regarding central pairs. Also, the H-bond pattern differed. Whereas S61-C63 interactions dominated for the *4LBS1* and *4LBS2* models, mixed S61-C63 and C63-C63 interactions were found for *4LBH1* and *4LBH2* models. Thus, the face-to-face interfaces differed in detail considerably between the models. However, the average H-bond count for all models of ~2 and the observation of shifts in the H-bond pattern, indicating a slide of the two β4-strands with respect to each other, were similar to the results of CLDN15 MD simulations [28]. Thus, the results are consistent with face-to-face-*cis* interface formation.

The hallmarks of the linear-*cis* interface are contacts between M69 and F146/F147/L158 and between S68/M69 and E157 (Fig. 1A, 2A; [10]). Thus, the linear-*cis* interface was analyzed by measuring the M69(C_ε)-L158(C_γ) distance over time and counting individual interfaces with at least one electrostatic interaction between S68/M69 and E157 over time. For all models, M69-L158 distance was relatively constant, for *4LBH1*, *4LBH2* and *4LBS2* around ~8 Å and for *4LBS1* around ~6 Å (Fig. 3B). The S68/M69-E157 interaction parameter was also relatively constant over time (~± 1) but differed for the models (~2.5 for *4LBS1* to ~7 for *4LBH2*) (Fig. 3C). Nevertheless, the values indicate that the linear-*cis* interface is maintained during the production run to a certain extent.

For the ECS2-ECS2-*trans* interface, P149-P149 proximity was suggested previously [15,24,25] and observed in the contact maps (Fig. 2C). Thus, the interface was evaluated by measuring the P149-P149 (C_α) distance over simulation time (Fig. 3D). Similar to the M69-L158 distance, P149-P149 distance for all models was relatively constant, for *4LBH1*, *4LBH2* and *4LBS2* around ~8 Å and for *4LBS1* around ~6 Å. This indicates similar ECS2-ECS2 positioning for all models. However, the full variability of this interface over time and between individual chain pairs is not in detail reflected by this analysis and beyond the scope of this study.

Next, contribution of the conserved β1β2 loop tip (V39, I40) to hydrophobic cluster formation was analyzed. *Trans*-proximity for these residues with hydrophobic V32/T44/W46 was indicated by the contact maps (Fig. 2G, I). In addition, *cis*-contacts between V39, I40 residues were suggested [15]. Respective distance measurements (C_β for V39, I40; $C_{\varepsilon 2}$ for W46) gave pairwise distances of mostly > 9 Å indicating on average no interaction (Fig. 3E). As a measure for hydrophobic clustering, water exclusion was analyzed by calculation of the solvent-accessible surface area (SASA). SASA values for V39/I40 of four interacting chains were 345–410 Å^2 for *4LBS1* and *4LBS2*. Thus, close to SASA range of four non-interacting chains at dodecamer periphery (∼600 Å^2). For *4LBH1* and *4LBH2*, SASA values were still 195–315 Å^2 (Fig. 3F). These high values do not support a clear contribution of the conserved β1β2 loop tip to formation of a hydrophobic cluster that was proposed earlier [15].

In addition, hydrophilic residues in the β1β2 loop (D36, T38) were suggested to contribute to electrostatic networks that potentially stabilize interaction between multiple chains [15,33]. Due to experimental data and modeling, we hypothesized that interaction of D36 or T38 with K64 might, on the one hand, stabilize oligomerization and, on the other hand, keep the positively charged K64 away from the center of the cation pore [15,33]. Indeed, the contact maps show that these residues are in some proximity (Fig. 2D). A respective interaction analysis revealed that K64 was often oriented away from the pore center over time by inter-chain interactions with D36, T38 and/or the nearby T58 of the β3β4 loop. However, K64 was also partly oriented towards the pore center by interaction with D56/N62 of the same or face-to-face interacting chain (Fig. 3G). The mentioned interactions differed also between the models. The data suggests a considerable flexibility of K64.

A high variability was also observed for orientation of D36 of the β1β2 loop. It did not only partly *trans*-interact with K64 (Fig. 3G), but also in *trans* or within the same chain with K155 (Fig. 3H). The extent of this interaction differed between the models. When present, it interfered with/influenced the ECS2-ECS2-*trans* interface.

In sum, the results underlined that all interface types were maintained during simulation of the *4LB* models, though a considerable variability and unexpected high SASA for β1β2 loop tips was observed.

3.2.4. Ion permeation pathway of pore in CLDN10b tetrameric-locked-barrel models

For characterization of the ion permeation path, the diameter along the pore axis of the central pore in the dodecamer was analyzed for the last 20 ns of the simulation using the HOLE program (http://www.holeprogram.org/). For all models, the narrowest pore region was located in the pore center, close to a ring of four D56 residues, each contributed by one chain of the tetramer (Fig. 4A). The precise position of the constriction site differs slightly between the models. The widest region was at the pore entrance close to D73 and D148. However, the diameter at a given distance from the center differed between the models and partly also between the two sides of the pore indicating flexibility and/or limited precision of the simulations. The mean minimal diameter for three models (*4LBH1* ∼5.1 Å, *4LBS2*, 4.3 ∼Å, *4LBH2* ∼4.0 Å) was in the experimentally measured range of ∼4 to ∼5.2 Å [33,49].

As an example, the pore of the *4LBH2* model is shown in more detail (Fig. 4B, C; see also Fig. S5 with similar results for *4LBS2* model). The lining of the central pore (∼60 Å in length) was formed nearly completely by four chains, only (*tetrameric-locked-barrel*). The pore center (loaded with Na$^+$) was lined by D56, S57, T58 and N62 of four chains, suggesting that these hydrophilic residues form the charge selectivity filter of CLDN10b channels. This fits to previous studies showing that D55 of CLDN15 that corresponds to D56 in CLDN10b, determines charge selectivity [25,33,50]. In contrast, D65 – the other negatively charged residue in ECS1 specifically shared

between CLDN10b and −15 – was mainly oriented away from the pore center, suggesting no direct interaction with permeating ions. Other negatively charged residues lining the pore on both sides of the center towards the entrance were D36, E153 and E145 (Fig. 4). E157 was mainly integrated in the linear-*cis* interface (Fig. 2), whereas D73 and D148 were located at the entrance.

Interestingly, K64 was located close to the pore center (Fig. 4) and showed flexible interactions with D36, D56, N62, or D65 during the simulation (Fig. 3G; Fig. 4B, C). This indicates that K64 influences the ion passage also.

3.3. MD simulations of CLDN15 tetrameric-locked-barrel models showed similar results as those for CLDN10b

MD simulations of the CLDN15 *tetrameric-locked-barrel* models showed similar results as those of CLDN10b concerning most of the key features: overall arrangement, stability/variability of the different interface types, contact map patterns, minimal pore diameter and gross orientation of most of the pore-lining residues (Fig. 5). Differences were obtained with respect to the hydrophobic β1β2 loop tip. The mean closest distance of I39-I39 for CLDN15 was 4.8 ± 1.0 Å, by tendency smaller than the one of the corresponding CLDN10b value of 6.2 ± 1.1 Å for I40-I40 (contact map data). Furthermore, the mean SASA for V38/I39 clusters was with 137 ± 36 Å^2 (Fig. 5H, mean of 8 values) lower than the corresponding CLDN10b value of 310 ± 85 Å^2 for V39/I40 (Fig. 3F, mean of 8 values).

In sum, on the one hand, the CLDN10b and CLDN15 data supported the JDR arrangement of the claudin channels to a large extent. However, on the other hand, the following results raised questions about the validity of the proposed *tetrameric-locked-barrel* model:

(i) The structural variability in detail **(ii)** The high SASA values of the β1β2 loop tip - especially for the CLDN10b models. This did not robustly support formation of a hydrophobic cluster of the loop tip as suggested previously [15] **(iii)** The minimal pore diameter that was similar for CLDN10b and -15 models. This did not fit to experimentally determined differences in the size-selectivity of these two channels [25,33,49].

Consequently, alternative CLDN10b models were also generated.

3.4. Generation of octameric-interlocked-barrels dodecamer models (8IB) for CLDN10b

For CLDN15 channels, Samanta et al. suggested a model that was also based on Suzuki's JDR arrangement [25] and contained a β1β2 loop orientation that differed from the *tetrameric-locked-barrel* model (*4LB*) suggested for CLDN10b [15]. In the *4LB* model, the β1β2 loop shows a straight extension/orientation towards chains in the opposing membrane (Fig. 6A). In contrast, in Samanta's model the β1β2 loop shows a more kinked/flat orientation towards a chain in the same membrane. This results in an *octameric-interlocked-barrels*-like conformation of the pore (*8IB* model, Fig. 6B). To compare the two models differing in β1β2 loop orientation, also *8IB* CLDN10b models were generated (Fig. S2). Based on Suzuki's CLDN15 oligomer template, a β1β2 loop conformation predicted by AlphaFold [31,32] and CLDN10b homology models, a CLDN10b dodecamer model was generated, embedded in two POPC membrane, relaxed, equilibrated and further simulated as described in the methods. The second last simulation step was performed for 100 ns with weak constraints on the linear-*cis* interface, only (*8IBli* model). The last step was done for 100 ns without constraints (*8IBno* model). In addition to the *8IBno* model, the *8IBli* model was also analyzed in detail to test whether stabilization of the proposed linear-*cis* interface increases stability/plausibility of the rest of the CLDN10b dodecamer model.

As an example, 100 ns snapshot of the CLDN10b *8IBno* simulation is shown (Fig. 6C-G). Concerning the overall arrangement, the model
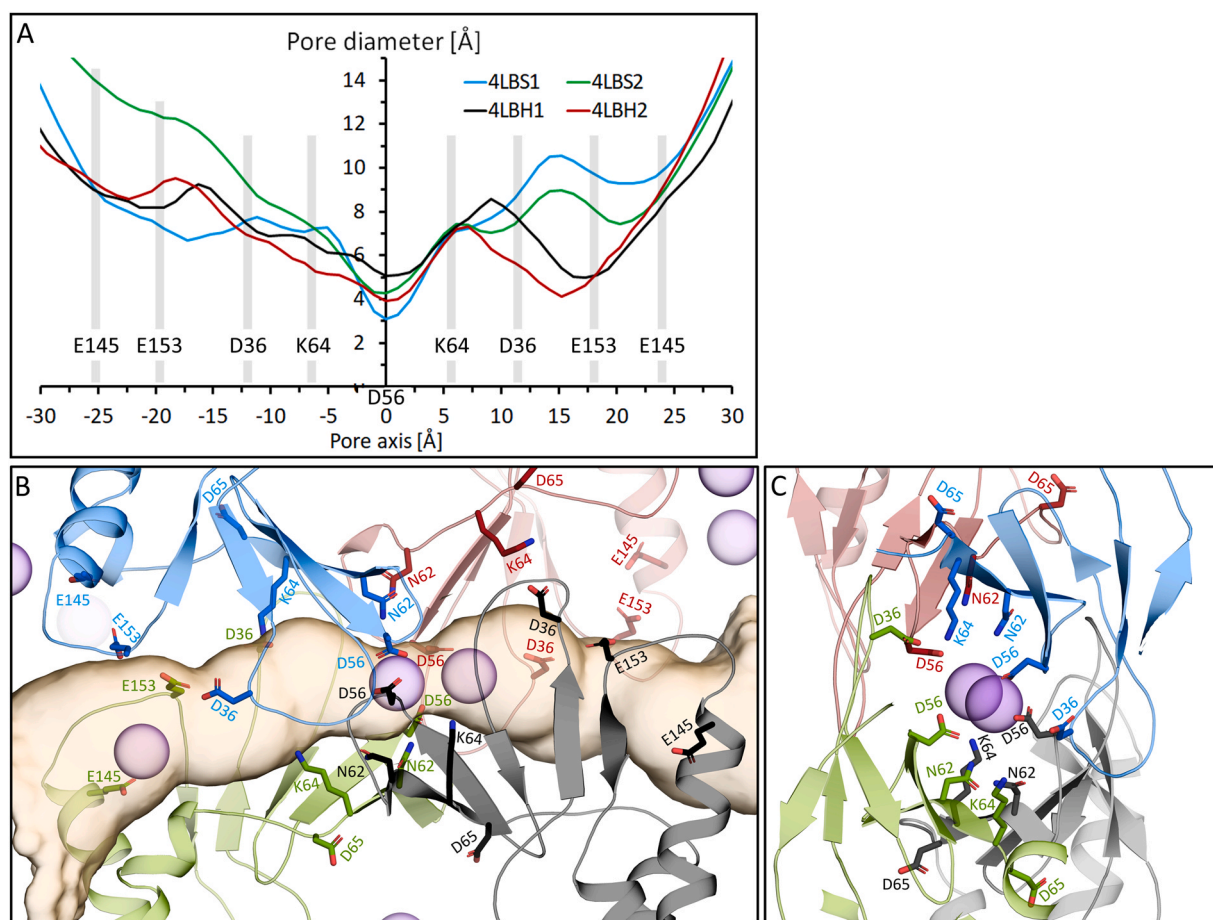
Fig. 4. Ion permeation pathway of pore in CLDN10b *tetrameric-locked-barrel* models. (A) Pore diameter profiles. Mean diameter of last 20 ns of simulation along the pore axis is shown. Pore pathway and diameter detection by HOLE program. Position of most relevant residues along pore axis are indicated. (B) Snapshot at 100 ns of production run, *4LBH2* model. Chains of central tetramer are shown (differently colored cartoons). Most relevant pore lining residues are shown as sticks. Pore axis is oriented similar to (A). Permeation pathway determined by HOLE is shown as transparent beige surface, Na⁺ as spheres. (C) Central tetramer, view turned by 90° with respect to (B).

was similar to the CLDN10b *4LB* models. The chains were embedded well in the membrane and the lipids in the central region between the two claudin rows were trapped, suggesting a special lipid micro domain around claudins (Fig. 6C, D). All interface types (linear-*cis*-, face-to-face-*cis*-, ECS2-ECS2-*trans* interfaces and central β1β2 loop cluster) were largely maintained and the open β-barrel-like pore was preserved (Fig. 5E-G). However, individual interfaces varied in detail to a certain extent. In the following, the MD simulations of the *8IBli* and *8IBno* models were evaluated and compared in detail.

3.5. Evaluation of the CLDN10b 8IB models

3.5.1. RMSD indicates overall stability of the dodecamer models

To evaluate the oligomer stability, RMSD of the protein backbone with respect to the initial structure was calculated for central tetramer chains of the *8IBli* and *8IBno* models. The mean RMSD over the last 50 ns of simulation was for *8IBno* < 1.5 Å and *8IBli* < 1.0 Å - both lower than those of the *4LB* models - indicating overall stability of the membrane-embedded oligomers (Fig. S6A). The secondary structure of the claudin chains was well-preserved in average (Fig. S6B). For both models, the RMSF of the central tetramer backbones was for most residues ∼ ≤ 1 Å, and especially for *8IBli* slightly smaller than for the *4LB* models, further indicating stability. However, in addition to the intracellular regions, the RMSF was higher for the ECS2 (up to 2.25 Å) indicating higher structural variability in these regions (Fig. S6B).

3.5.2. Defining the 8IB dodecamer inter-chain interfaces by residue contact maps

As for the *4LB* models, inter-chain residue contact maps were created as fingerprints for the *8IB* models. Similar to the *4LB* models, the maps for *8IBli* and *8IBno* models fit to the JDR arrangement of claudins within strands. For the *8IBno* model, interaction-relevant regions of the contact maps are shown (Fig. 7).

For linear-*cis* interface, closest distances were found for M69 with I142/T143/F146/Y156/E157/L158 and S68 with E157/L158. In addition, contact between L72 and L158 and proximity between D65 to S68 with T34/I35 was detected (Fig. 7A, linear-*cis* map). For face-to-face-*cis* interface, closest distances were found between the residue pairs 62/63, 63/63, 63/61, 64/61 (Fig. 7B, face-to-face map). ECS2-ECS2-*trans* closest distances were found between P149 and F146 to P149, F146 and L150 to K155 and K155-K155 (Fig. 7C, ECS2-ECS2-*trans* map).

Key differences to the *4LB* models were detected in the pattern in which the β1β2 loop contacted its counterpart and the β3β4 loop in *cis* or *trans*. The following close β1β2 loop contacts were detected. *Trans*-pairs in one claudin row: T38/V39/I40 with T38/V39/I40 and A43/T44/Y45 (Fig. 7 G, β1β2β3β4_linear_*trans* map); *trans*-pairs between rows: I40 with V39/I40 (Fig. 7I, β1β2β3β4_*trans*_ftf map); *cis*-crosswise between rows: I40/T41/T42 pairs (Fig. 7H, β1β2β3β4_*cis*_crosswise map).

As β1β2 loop to β3β4 loop contacts, S33 to A43 region with S57 to V60 region was detected in the β1β2β3β4_*cis*_crosswise map (Fig. 7H) and T44/Y45 with S57/T58 in the β1β2β3β4_*trans*_ftf map
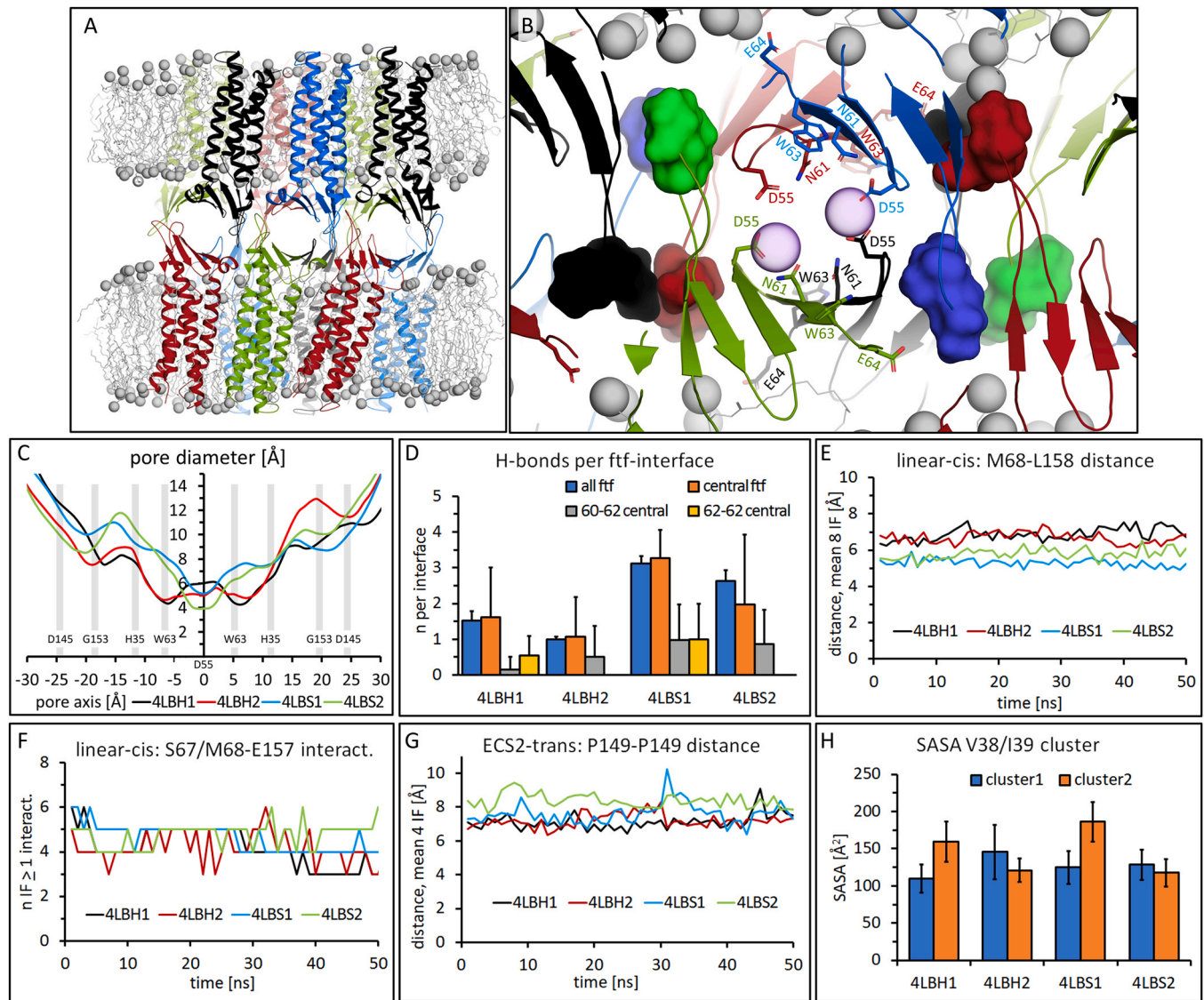
Fig. 5. MD simulations of CLDN15 *tetrameric-locked-barrel* models showed similar results as those for CLDN10b. (A) As an example, 15_*4LBS1* model is shown. Snapshot at the end of 60 ns production run. Claudin chains of dodecamer are well embedded in membranes. Side view, protein chains shown as colored cartoon, POPC lipids as lines and phosphates as beige spheres. **(B)** Close up of dodecamer center. β1β2 loop cluster: between the pores, hydrophobic V38/I39 residues (shown as surface) at β1β2 loop tip of two chains are in close *cis*-proximity (black – red, green – blue). In contrast, no *trans*-contact is given between the tips (black/red – green/blue). The central pore is shown in more detail. In its center, only Na^+ but no Cl^- ions are present, demonstrating the expected charge selectivity of the modeled channels. Most-relevant pore lining residues in pore center are shown as sticks. Similar to the corresponding residues of CLDN10b, four D55 from four chains are oriented towards pore center and interact with Na^+, whereas E64 points away from the pore towards the lipid head groups. The non-charged W63, corresponding to K64 in CLDN10b, lines the pore, too. **(C-H)** Further analysis for CLDN15 *tetrameric-locked-barrel* models *4LBH1*, *4LBH2*, *4LBS1* and *4LBS2*. **(C)** Pore diameter profiles. Mean diameter of last 20 ns of simulation along pore axis is shown. Pore pathway and diameter detection by HOLE program. Position of most relevant residues along pore axis are indicated. Minimal pore diameters were in a similar range as those for the CLDN10b *4LB* models. **(D)** Face-to-face-*cis* (ftf) interface: T57 to E64 backbone H-bond counts per interface, for all six (all) and central two (central) interfaces of dodecamer. In addition, counts for 60–62 and 62–62 residue pairs for central interfaces. The H-bond counts differed between the models. Mean ± SD. **(E)** Linear-*cis* interface: M68($C_ε$)-L158($C_γ$) distances over time. Mean of eight interfaces in dodecamer. **(F)** Linear-*cis* interface: number of interfaces (IF, out of eight) with ≥ one S67/M68-E157 (side & main chain) electrostatic interaction count over time. **(G)** ECS2-*trans* interface: P149($C_α$) - P149($C_α$) distances over time. Mean of four interfaces in dodecamer. **(H)** β1β2 loop cluster: SASA for V38/I39 of four interacting chains, two clusters for each dodecamer model. Mean ± SD.

(Fig. 7I). Further proximities for β1β2 loop residues were found between S37/T38 and Q154 in ECS2 (β1β2 loop-ECS2_*trans* map, Fig. 7F) and T32 and E157 in ECS2 (β1β2 loop-ECS2_same chain map, Fig. 7E).

In sum, the contact maps provide detailed contact fingerprints defining the interfaces. In particular, the maps clearly display the β1β2 loop interaction patterns differing between the *4LB* and *8IB* models.

3.5.3. Further analysis of interfaces in 8IBli and 8IBno models

The *8IBli* and *8IBno* models were further analyzed regarding the different interface types. For the face-to-face-*cis* interface, mean H-

bonds between two β4-strand regions (T58 to D65 residue backbones) were counted (Fig. 8A). For all six chain pairs in the dodecamer, the mean H-bond count per interface was ~2 for both models. For the central pairs, it was ~2 for *8IBli* and ~1 for *8IBno*. In sum, the H-bond counts were in a similar range as those of the *4LB* models (Fig. 3A). However, in contrast to the latter, only C63-C63 but no S61-C63H-bonds were detected. Thus, the H-bond pattern was similar to the main pattern reported for CLDN15 simulations [24,25].

The linear-*cis* interface was analyzed by measuring the M69($C_ε$)-L158($C_γ$) distance over time and counting individual interfaces with at least one electrostatic interaction between S68/M69 and E157 over time. For *8IBli*, the M69-L158 distance was more constant than
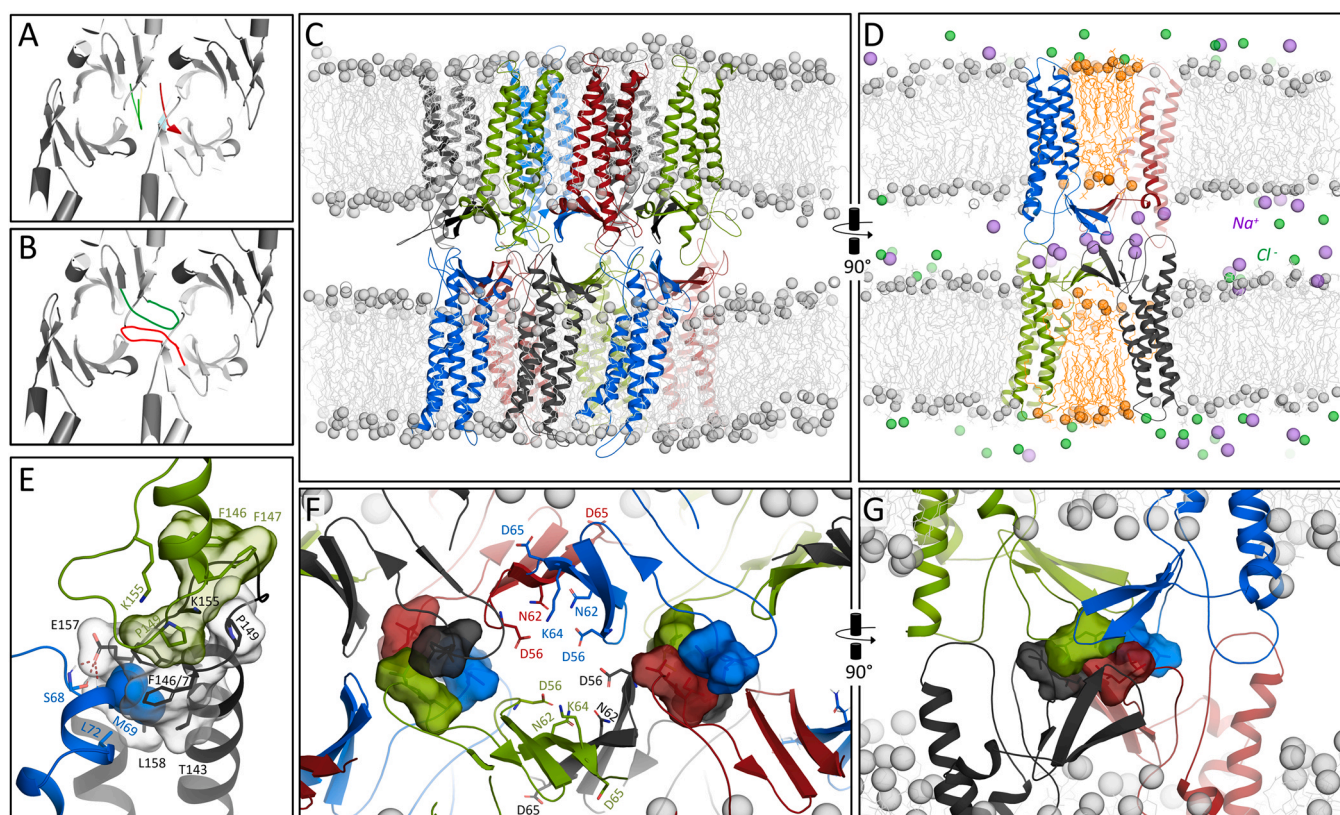
Fig. 6. (A, B) Schema highlighting different orientation of β1β2 loop in *tetrameric-locked-barrel* (*4LB*) and *octameric-interlocked-barrels* (*8IB*) models. Two out of four β1β2 loops (colored) between two pore barrels (gray) are shown. (A) In *4LB* model, β1β2 loops show straight extension/orientation towards chains in opposing membrane. (B) In *8IB* model, β1β2 loops show more kinked/flat orientation towards chains in the same membrane. (C-G) CLDN10b_*8IBno* model after MD simulation. Snapshot of production run at 100 ns. (C) Side view, claudin chains shown as colored cartoon, POPC lipids as lines and phosphates as spheres. (D) Turned-view on central pore. In membrane between the two claudin rows, lipids (orange) are trapped. In pore center, only Na⁺ (magenta spheres) but no Cl⁻ (green spheres) ions are present, demonstrating expected charge selectivity of the modeled channels (See also Fig. S3 I-M). (E) Close up of linear-*cis* and ECS2-ECS2-*trans* interfaces. M69 (spheres) of blue chain sticks in pocket of gray chain formed by T143, F146, F147, E157, L158 shown as gray sticks and surface; E157-S68/M69H-bonds shown as dashed lines; F146, F147 and P149 contributing to *trans*-interaction shown as gray and green sticks and surfaces. (F) Close up of dodecamer center. Hydrophobic cluster formation on both sides of central pore by hydrophobic V39 & I40 residues (surfaces) at β1β2 loop tips of four chains (green, blue, black, red). V39/I40 are in close *cis*- and *trans*-contact, in contrast to the *4LB* models (see Fig. 1D, G; Fig. 5B), Most relevant residues of central pore are shown as sticks. (G) Turned-view highlighting right V39/I40 cluster of (F).

for *8IBno* (Fig. 8B). However, for both, *8IBli* and *8IBno*, it was ∼5.5 Å, slightly lower than for *4LB* models (Fig. 3B). S68/M69-E157 interaction parameter was also constant over time (∼± 1), for *8IBno* ∼5 and *8IBli* ∼4 (Fig. 8C) and in between the values for different *4LB* models (Fig. 3C). Thus, the values indicated that the linear-*cis* interface is largely maintained for not only the *8IBli*, but also for the *8IBno* model.

For the ECS2-ECS2-*trans* interface, P149-P149 (C$_α$) distance over simulation time was measured. It was relatively constant (∼8.5 Å) for *8IBli*, and for *8IBno*, a lower value of ∼6.7 Å with slightly higher variability was observed (Fig. 8D). The latter was slightly lower than P149-P149 distance of most of the *4LB* models (Fig. 3D). The data indicated that ECS2-ECS2 proximity was maintained during the *8IB* simulations.

Next, contribution of the β1β2 loop tip (V39, I40) to hydrophobic cluster formation was analyzed. For comparison with the *4LB* models, the mean pairwise distances for V39-V39, I40-I40, V39-I40, I40-V39 (*cis*, C$_β$-atoms) and I40-W46 (*trans*, C$_β$ for V39, I40; C$_{ε2}$ for W46) were calculated (Fig. 8E). For I40-I40, the distance was much lower (∼6.3 Å for *8IBli*, ∼6.6 Å for *8IBno*) but for I40-W60 much higher (both models ∼14.7 Å) than the respective distances for the *4LB* models (Fig. 3E). These values underlined that the β1β2 loop interaction pattern differed strongly between the *8IB* and *4LB* models. As a measure for hydrophobic clustering, water exclusion was analyzed by calculation of the SASA. SASA mean values for V39/I40 of four interacting chains were 67.1 ± 14.9 and 70.4 ± 8.2 Å² for *8IBli*, and 48.8 ± 11.2 Å² and 50.5 ± 13.3 Å² for *8IBno* clusters

(Fig. 8F), much lower than the SASA for the clusters in the *4LB* models (195–411 Å², Fig. 3F). These results showed that hydrophobic cluster formation by V39/I40 was much stronger for the *8IB* than for the *4LB* models.

Furthermore, electrostatic interactions of charged residues located close to the pore center were investigated for *8IBli* and *8IBno*. K64 interacted partly with D56/N62 in pore center or partly away from it with D36 or other residues close-by indicating flexibility of the K64 orientation (Fig. 8G). In contrast to the *4LB* model (Fig. 3H), D36 did not interact with K155 of ECS2 (Fig. 8H).

3.5.4. Ion permeation pathway of pore in CLDN10b octameric-interlocked-barrels models

For characterization of the ion permeation path, the diameter along the central pore axis was analyzed in the last 20 ns of the simulation (using HOLE). For both models (*8IBli* and *8IBno*), the widest region was at the pore entrances close to D73 and D148 residues; the narrowest region was in the pore center, close to the ring of four D56 residues from the four central chains (Fig. 9). The mean minimal diameter for *8IBli* was ∼4.0 Å and for *8IBno* ∼5.2 Å, both in the experimentally measured range of ∼4 to ∼5.2 Å [33,49]. For the constriction site, not only size, but also precise position and spread along pore axis differ between the two models to a certain extent (Fig. 9A). The diameter at positions between D56 and E153 residues differed between both models and both sides from the center. This
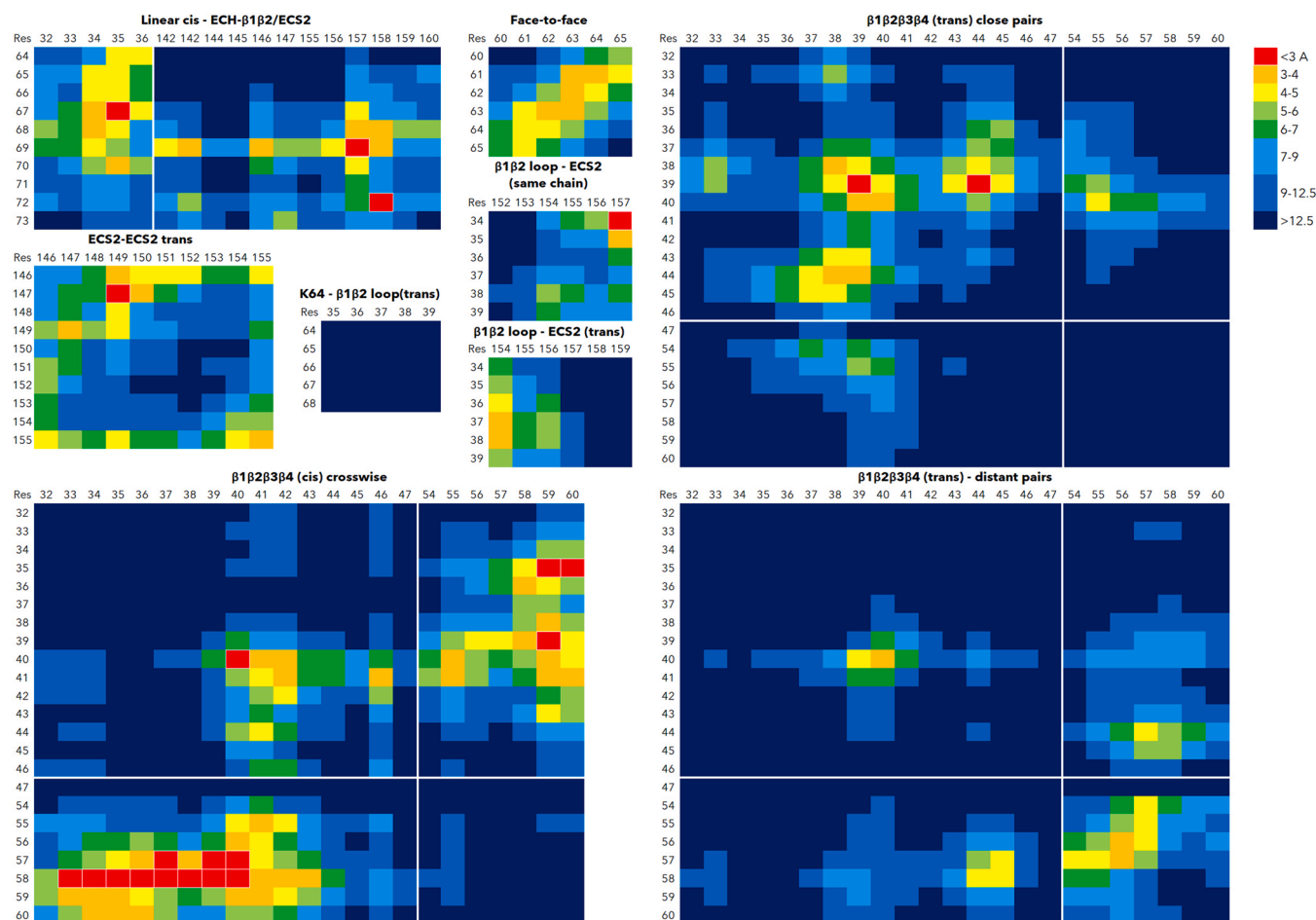
Fig. 7. Inter-chain contact maps for the CLDN10b *octameric-interlocked-barrels* model *8IBno*. Mean distances (closest atoms) between the numbered residues of protein region pairs reflecting the different interface types. For each interface type, multiple individual interfaces in the dodecamer were averaged. Shown are interaction-relevant parts of contact maps (containing regions with distances < 9 Å and/or parts to be compared) categorized according to the interface types. **(A)** Linear-*cis*. **(B)** Face-to-face-*cis*. **(C)** ECS2-ECS2-*trans*. **(D-F)** β1β2 loop with neighboring K64-region and ECS2. **(G-I)** Central cluster of β1β2β3β4 loops, three different chain pairs. For definition, see headlines and chain numbering of Fig. 1B, D. The contact maps provide interface fingerprints for the CLDN10b *8IBno* model.

indicated flexibility of the pore and/or a limited precision of the simulations.

In contrast to the *4LB* models, pore lining of the central pore (~60 Å in length) was formed by more than the four central chains (*octameric-interlocked-barrels*). The pore center (loaded with Na⁺) was lined by D56, S57, N62 and partly T58 of four chains, suggesting that these hydrophilic residues form the charge selectivity filter of CLDN10b channels (Fig. 9C). Similar to the *4LB* models, this fits to previous studies [25,33,50]. Also similar to the *4LB* models, D65 was oriented away from the pore center, whereas other negatively charged residues D36, E153 and E145 lined the pore on both sides from the center towards the entrances. In contrast to the *4LB* models, D36 belonged to neighboring, non-central chains. Similar to the *4LB* models, K64 located close to the pore center and showed flexible interactions with D36 or D56/N62 (Fig. 8G), indicating that also this positively charged residue could influence the ion passage.

3.6. Comparison of the tetrameric-locked-barrel (4LB) and octameric-interlocked-barrels (8IB) models

For comparison of the *4LB* and *8IB* models, key results are summarized in Table 1. Charge-selective paracellular ion channels as demonstrated by electrophysiological studies [33,51] were obtained for both models (Fig. S3). Also for both model variants, the linear-*cis* and face-to-face-*cis* interfaces as well as ECS2-ECS2 contacts showed considerable fluctuations (Figs. 3A-D, 8A-D, 5D-G). However, they

were all largely maintained throughout the simulations. Face-to-face H-bond pattern (Fig. 3A, 8 A) of the *8IB* models fitted better to previous reports [15,24,25]. Structural variability over time (RMSD/RMSF) was lower for *8IB* (Fig. S4A, S6A). Although the pore profiles differed in detail between the six individual models, the observed pore asymmetries and minimal pore diameters were comparable for the *4LB* and *8IB* CLDN10b models (Figs. 4A, 9A, S7). However, the expected difference in size of the CLDN10b and − 15 pores [33,49] could not be observed for the *4LB* models (Fig. 4A, 5C). D36 was robustly oriented towards the pore and did not affect the ECS2-ECS2-*trans* interface only for *8IB* (Figs. 3H, 8H). In addition, for *8IB*, proximity between T38 and Q154 was observed (Fig. 7E-F). This provides a potential explanation for covariance of polar residues at these positions among vertebrate CLDN10b/- 15-like sequences (data not shown). Furthermore, contacts between the hydrophobic V39/I40 residues and the corresponding water exclusion (SASA) was much closer/stronger for *8IB in comparison to 4LB* models (Figs. 2G-I, 3E-F, 7G-I, 8E-F). In sum, the data provide more support for the *8IB* model. Thus, the latter was further analyzed in more detail.

3.7. Interaction of pore-lining residues with Na⁺ in the octameric-interlocked-barrels model

In order to analyze the contribution of CLDN10b-specific pore-lining charged residues to ion permeation, two CLDN10b mutant models were generated using the membrane-embedded *8IBli* model
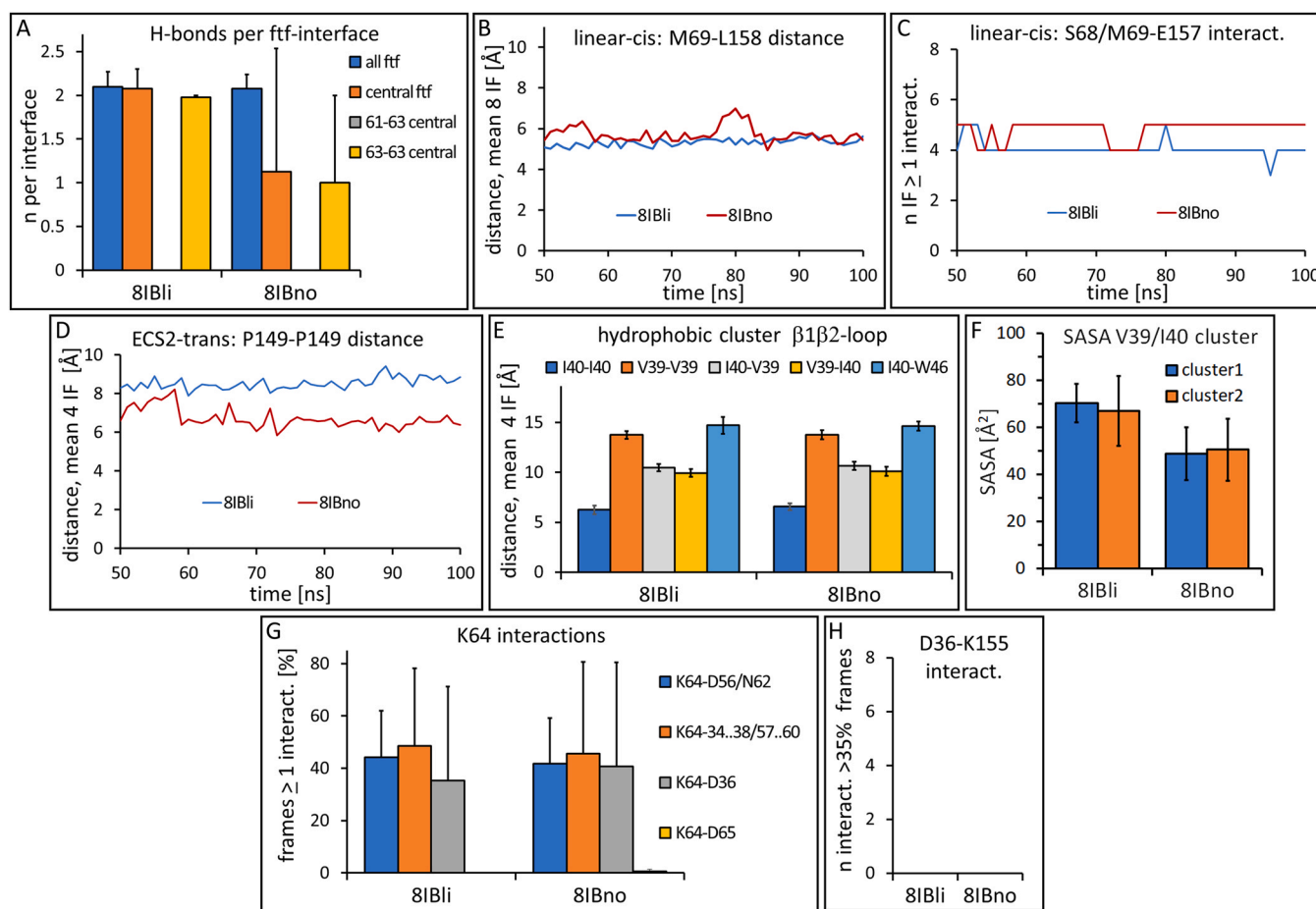
Fig. 8. Detailed interface analysis for CLDN10b *octameric-interlocked-barrels* **models** *8IBli* **and** *8IBno*. **(A)** Face-to-face-*cis* (ftf) interface: T58-D65 backbone H-bond counts per interface, for all six (all) and central two (central) interfaces of dodecamer. In addition, counts for 61–63 and 63–63 residue pairs of central interfaces. Mean ± SD. **(B)** Linear-*cis* interface: M69(C_ε)-L158(C_γ) distances over time. Mean of eight interfaces in dodecamer. **(C)** Linear-*cis* interface: number of interfaces (IF, out of eight) with $\geq$ one S68/M69-E157 (side & main chain) electrostatic interaction count over time. **(D)** ECS2-*trans* interface: P149(C_α)-P149(C_α) distances over time. Mean of four interfaces in dodecamer. **(E)** β1β2 loop cluster**:** Pairwise distances for V39-V39, I40-I40, V39-I40, I40-V39 (*cis*, C_β-atoms) and I40-W46 (*trans*, C_β for V39/I40, $C_{\varepsilon2}$ for W46). Mean±SD of four (eight for I40-W46) interfaces in dodecamer. **(F)** β1β2 loop cluster**:** SASA for V39/I40 of four interacting chains, two clusters for each dodecamer model. Mean ± SD. **(G)** K64 orientation and interactions**:** % of frames with $\geq$ one interaction count for NH3+of K64 with following residues (side or main chain): (i) D56/N62 same or other chain, *cis*; (ii) T34 to T38, S57 to V60, *cis*; (iii) D36, *cis*; (iv) D65, same chain. Mean ± SD for four K64 in central tetramer. **(H)** D36 orientation: In contrast to *4LB* models, no D36-K155 pairs (*trans* or same chain, in total 16 in dodecamer) interacting in > 35% of frames were detected. For (A) the last 20 ns and (B-H) the last 50 ns of production runs were analyzed.
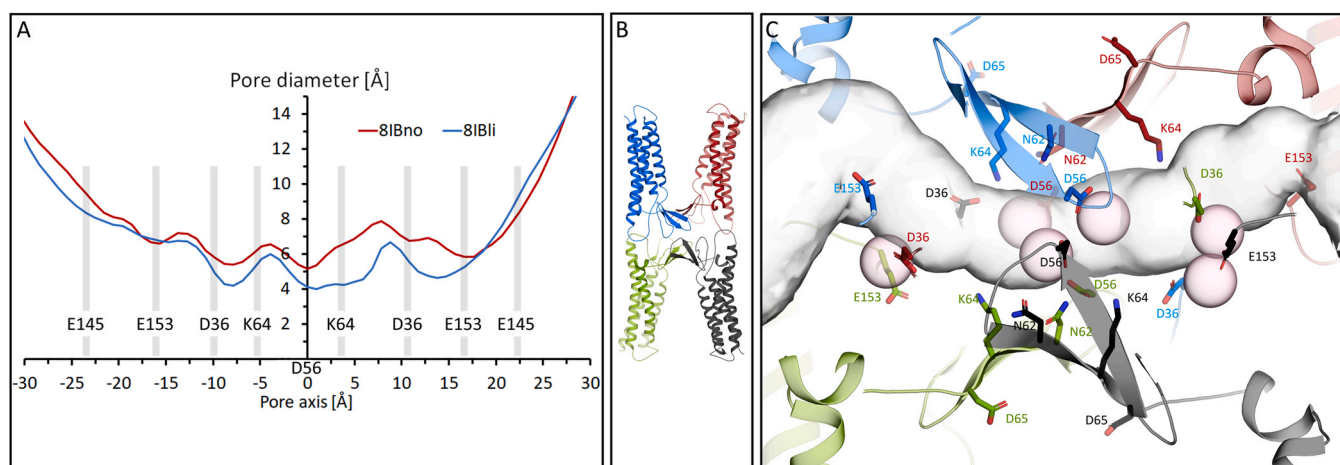
Fig. 9. Ion permeation pathway of pore in CLDN10b *octameric-interlocked-barrels* models. (A) Pore diameter profiles for *8IBli* and *8IBno* models. Mean diameter of last 20 ns of simulation along the pore axis. Pore pathway and diameter detection by HOLE program. Position of most relevant residues along pore axis are indicated. (B, C) Snapshot at 100 ns for *8IBno* model. Chains of central tetramer are shown as colored cartoon. (B) Overview, pore axis runs from left to right. (C) Close up of permeation pathway. Most-relevant pore lining residues are shown as sticks. D36 residues belong to neighboring, non-central chains (respective chain cartoons are hidden for clarity). Permeation pathway determined by HOLE is shown as transparent beige surface, Na+ as spheres. Appearance of Na+ (near E153), close to but outside the pore pathway determined by HOLE indicates partial underestimation of pore diameter, e.g., due to spherical diameter probing.

Table 1

Comparison of key parameters of *tetrameric-locked-barrel* and *octameric-interlocked-barrels* model variants.

Parameter	CLDN10b *tetrameric-locked-barrel* (*4LB*)	CLDN15 *tetrameric-locked-barrel* (*4LB*)	CLDN10b *octameric- interlocked-barrels* (*8IB*)
RMSD/RMSF	< 2 Å / < 1.5 Å, up to 2.7 Å (Fig. S4A)	n.d.	< 1.5 Å / $\leq$ 1 Å, up to 2.3 Å (Fig. S6A)
Linear-cis interface	maintained, flexible (Fig. 3B-C)	maintained, flexible (Fig. 5E-F)	maintained, flexible (Fig. 8B-C)
Face-to-face interface	maintained, ~2 H-bonds, more 61–63 than 63–63 pattern (Figs. 2B,3A)	maintained, ~2 H-bonds, mixed 61–63/63–63 pattern (Fig. 5D)	maintained, ~2 H-bonds, mainly 63–63 pattern (Figs. 7B,8A)
ECS2-ECS2-trans interface	contact maintained, flexible, partially affected by D36-K155 interaction (Fig. 3D, H)	contact maintained, flexible, no considerable H35-K155 interaction (Fig. 5G)	contact maintained, flexible, no D36-K155 interaction (Fig. 8D, H)
Charge selectivity of channel	Cations (Fig. S3D-H)	Cations (Fig. 5B)	Cations (Fig. S3I-M)
Pore diameter	~3.1–5.1 Å (Fig. 4A)	~3.9–5.2 Å (Fig. 5 C)	~4.0–5.2 Å (Fig. 9A, C)
D36 orientation	only partly towards pore (Fig. 4B, C)	H35 mainly towards pore	towards pore (Fig. 9C)
T38-Q154 distance (CLDN15:N37-T154)	*trans* > 9 Å, (Fig. 2F) same chain 7–9 Å,(Fig. 2E)	*trans* > 10 Å, same chain > 9.5 Å	*trans* 3–4 Å, (Fig. 7F) same chain 5–6 Å, (Fig. 7E)
V39, I40 proximities (V38, I39 for CLDN15)	*trans* > 9 Å, (Fig. 2G, I) *cis* 6 – 7 Å, (Fig. 2H)	*trans* ~10 Å, *cis* ~5 Å	*trans* < 3 Å, (Fig. 7G, I) *cis* < 3 Å, (Fig. 7H)
V39, I40 SASA	310$\pm$85 Å^2, (Fig. 3F, Ø)	137$\pm$36 Å^2	~59$\pm$10 Å^2, (Fig. 8F, Ø)

as template. CLDN10b_K64M was created to specifically remove the CLDN10b-specific positive charge close to the pore center. CLDN10b_D36H/A47E/A52S/Y45I/K64W/E153G was created to convert the charge distribution and neighboring residues within the pore to a CLDN15-like condition (Fig. S1). After equilibration, a 100 ns production run was performed. Here, low constraints were applied on linear-*cis* interface (similar to *8IBli*) to slightly support the stability, which could have been affected by the mutations. The overall structure of the mutants was similar to that of CLDN10b_wt, indicated by low RMSD with respect to CLDN10b_wt (*8IBli*): 1.6 Å for CLDN10b_K64M and 1.9 Å for CLDN10b_CLDN15-like. Also, for all three models, nearly only Na$^+$ but hardly any Cl$^-$ was present in the pore beyond the entrance region. Thus, the simulations successfully reconstituted the Na$^+$ over Cl$^-$ selectivity of CLDN10b and CLDN15-like channels. However, their differing pore diameter [49,51,52] was not yet reproduced by the CLDN10b_wt and CLDN15-mimicking mutants.

As a measure for the interactions of pore-lining residues with Na$^+$, we calculated the mean number of the respective interactions in the last 50 ns of the production runs (Fig. 10A). Firstly, for all three conditions (CLDN10b_wt, -K64M, -CLDN15-like), the central cluster of D56 from four chains interacted very strongly with Na$^+$, whereas D65 interacted hardly with any ion. This is consistent with the critical but differential contribution of these two CLDN10b/-15-specific negative residues to channel properties [25,33]. Secondly, the CLDN15-like mutant, and even more pronounced CLDN10b_K64M, showed a higher Na$^+$-interaction count for D56 than that of CLDN10b_wt. Located next to D56 (Fig. 10C, E), W64 of the CLDN15-like mutant interacted with Na$^+$, whereas K64 of CLDN10b_wt and M64 of CLDN10b_K64M did not (Fig. 10A). D36 and E153 of CLDN10b_wt and of CLDN10_K64M interacted moderately with Na$^+$, whereas H36 and G153 of the CLDN15-like mutant did (almost) not interact with Na$^+$. E47 of the CLDN15-like mutant interacted hardly and A47 of CLDN10b_wt and CLDN10b_K64M interacted not with Na$^+$. Finally, the interaction counts for E145 and D148 at the pore entrance for all three models were much lower than the counts in the center.

Together, the quantification indicated that (i) the positive charge of K64 reduces the interactions of the central D56 cluster with Na$^+$ by competition, (ii) the presence of D36 and E153 instead of H36, G153 and E47 increases the interaction with Na$^+$ in the pore, and (iii) the charge-distribution along the pore differing between CLDN10b

and -15 (Fig. 10B-E) affects attraction, density and passage of Na$^+$ (see also discussion).

4. Discussion

In this study, we investigated paracellular cation channels formed by CLDN10b regarding structure, ion passage and polymerization into TJ-like strands. Based on Suzuki's joined double rows arrangement model for CLDN15, homology modeling and MD simulations, we tested two dodecamer model variants differing in orientation of the ECS1 β1β2 loop: a *tetrameric-locked-barrel* (*4LB*) vs *octameric-interlocked-barrels* (*8IB*) model. The results support the *8IB* model in which adjacent, sidewise-unsealed tetrameric pore scaffolds are interlocked via the β1β2 loop. On the one hand, the loop contributes to lining of the ion conduction pathway. On the other hand, it mediates hydrophobic clustering between four chains and, together with ECS2, *trans*- and *cis*- interaction between chains of the adjacent tetrameric pore scaffolds. This oligomerization mechanism is proposed to be conserved between classic claudins. However, the charge-distribution along the pore differing between CLDN10b and -15 is suggested to be a key determinant for the cation- and water permeabilities that differ between the two claudins.

Different models of the claudin backbone of TJ strands with embedded paracellular channels have been reported [10,14,15,18–23,41]. The models differ regarding the claudins investigated, the input of (structural and functional) in vitro/in situ data and the *in silico* methodology on which they are based. The joined double rows (JDR) model of CLDN15 suggested by Suzuki et al. [14] is, after several extensive refinements [23–25,28] and extension to other classic claudins [15,26,41,53], the one that is supported most by experimental and modeling data [10]. However, the validity of the model, especially in detail is unclear. Model variants differing in the conjunction of neighboring pores in strands were suggested for CLDN15 ([24] (*4LB*-like); [25] (*8IB*-like)) and for the closely related CLDN10b ([15]; *4LB*). In the current study, we refined and extended the *4LB* model to CLDN10b and CLDN15 dodecamers, created an *8IB* model for CLDN10b and compared the models using MD simulations of double membrane-embedded proteins.

For all models (Fig. S2), overall arrangement, inter-chain interfaces, and an open pore conformation were maintained. Nonetheless, the *8IB* model showed better characteristics concerning the face-to-face-*cis* and ECS2-ECS2-*trans* interface, other interface- and pore-lining residues, RMSD over simulation time and water
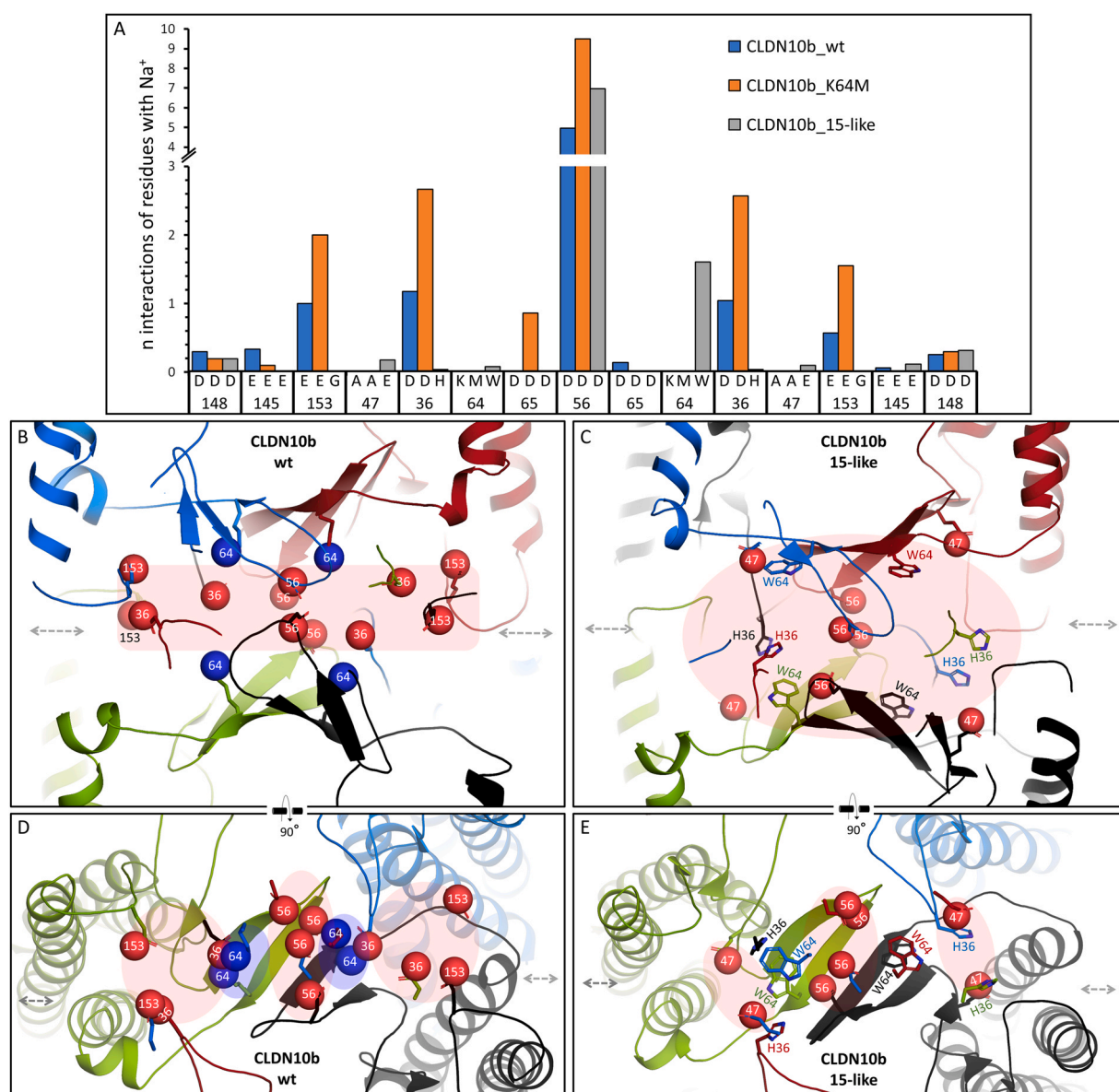
Fig. 10. Interaction of Na⁺ with residues lining the central pore in CLDN10b_wt, CLDN10b_K64M and CLDN10b_15-like mutant models. (A) Na⁺-interaction counts for the indicated residues and claudin models. Mean electrostatic interactions per 1 ns frame of 100 ns production runs. Models based on CLDN10b *8lBli*. (**B, C, D, E**) Snapshots at 100 ns, relevant residues (numbered) are shown as sticks with their charged atoms as red (-) or blue (+) spheres. Pink shading indicates negative, blue shading positive regions. Ion entrance/exit regions indicated by dashed arrows. (**B, C**) The eight chains of both membranes contributing to central pore are shown as colored cartoon, clipped to the central pore. (**D, E**) Top views, only the four chains in lower membrane contributing to central pore are shown as colored cartoon. Relevant residues from chains in upper membrane are shown as sticks and spheres. The distribution of charged residues along the pore differs for CLDN10b_wt (B, D) and CLDN15-like mutant (C, E). Number and density of negatively charged residues is higher for CLDN10b_wt (B, D) than for CLDN15-like mutant (C, E). For CLDN10b_wt, K64 bridges the negatively charged D56 cluster in center with D36 located apart from pore center.

exclusion mediated by interactions between V39/I40 residues. Especially the latter is of importance since presence of these hydrophobic residues at the tip of the flexible β1β2 loop correlates very strongly with the capability of claudins to form polymeric TJ-like strands [5,10]. Thus, driving polymerization of claudins by hydrophobic clustering provides an adequate explanation for the mentioned sequence conservation. Previous studies mentioned hydrophobic interactions of the β1β2 loop but did not show them explicitly and emphasize rather variability than conservation of this region and its involvement in H-bonding [25,29]. Hydrophilic interactions of β1β2 loop residues were observed (Fig. 7; Fig. 8G and data not shown). However, these are indeed expected to vary between claudins and are also predicted to be involved in heterophilic compatibility.

Originally, clustering of β1β2 loops was proposed as part of the *4LB* model for CLDN10b and CLDN3 [15]. However, the more detailed MD simulation of membrane-embedded dodecamers presented here showed more efficient clustering and water exclusion for the *8IB* model. The initially proposed β1β2 loop conformation was strongly based on Cys-scanning crosslinking data mainly obtained for CLDN3 [15]. The now observed discrepancy could be at least partially due to different β1β2 loop conformation for CLDN3 and −10b. In addition, some of the crosslinks between claudin residues could have been the result of random associations of the membrane proteins outside TJ-like strands. Nevertheless, part of the crosslinking data is also strikingly consistent with the *8IB* model (e.g., CLDN3-I39C dimer, CLDN10b-N62C dimer, [15]). However, currently, the *4LB* model cannot fully be ruled out. Of note, the large SASA in the *4LB* models is largely due to the exposure of V39/I40 to solvated POPC head groups.

Instead, local accumulation of lipids with uncharged head groups (e.g. cholesterol [54] or very long chain ceramides [55]) in the micro domain between claudin chains (Fig. 1F) might support the *4LB*-like close positioning of the hydrophobic β1β2 loop tip. However, this is speculation. In sum, overall comparison of the *4LB* and *8IB* models clearly favors the latter.

Both models successfully showed cation selectivity (Fig. S3) reflecting the experimental findings of CLDN10b and CLDN15 channels [33,50,51,56]. In addition, the pore diameter of the simulated CLDN10b channels is clearly smaller than the one of reported CLDN15 models [14,24,25], fitting well to experimental data [33,49,51,52]. However, the *4LB* and *8IB* models reported here could not yet reproduce the bigger sized CLDN15 pore. For the *4LB* models, this might be at least partly related to the unfavored orientation of the β1β2 loop. For the *8IB* model of the CLDN15-like CLDN10b mutant, it could be due to sequence differences between the two claudins other than the substituted residues (D36H/A47E/A52S/Y45I/K64W/E153G). However, the discrepancy could also be caused by a limited accuracy of the models, indicated also by a heterogeneity within the dodecamers obtained to a certain extent. Detailed refinement and increase of simulation time can further improve the accuracy of the models in further studies.

At this point, the simulations cannot completely rule out that native CLDN10b polymers in cells adapt another architecture than the one suggested here. However, for the related CLDN15, a recent remarkable study simulated polymers up to ~300 chains for up to 1 μs at hybrid resolution. Strikingly, stability/integrity was maintained even though considerable interfacial flexibility was detected [28]. This flexibility was associated with lateral bending of the polymers. These polymers were also based on Suzuki's JDR arrangement and an *8IB*-like pore scaffold [25,28]. Thus, it is plausible that the flexibility observed in the simulations presented here are at least partly due to an inherent flexibility of claudin inter-chain interfaces related to strand bending, branching, breaking (leak pathway) or channel gating. Together, the simulations strongly support an *8IB*-like JDR arrangement for at least the CLDN10b/-15 subgroup of claudin strands. Due to the high conservation of the participating interfacial residues (for linear-*cis*, face-to-face-*cis*, ECS2-ECS2-*trans* and β1β2 loop *cis/trans* cluster) among classic claudins [10,12], we propose a similar arrangement also for the other classic claudins. Nevertheless, not only the detailed interfacial conformations, but also the precise orientation of chains relative to each other could slightly but significantly differ, for instance to close the pore region for barrier-forming claudins. Alternative non-JDR arrangements suggested for oligomers of classic claudins [18,20–22] might be rather involved in branching of strands.

Based on Suzuki's CLDN15 model, a β-barrel-like tetrameric pore scaffold has been widely assumed for channel-forming claudins [14,15,24,53], although alternative tetrameric pore structures have been suggested, too [21,23,53]. The oligomeric channels have to be stringed together to form the polymeric backbone of TJ strands. *Cis-/trans*-tetramers have been suggested to form these building blocks of polymers for channel-forming as well as for barrier-forming claudins [15]. While in the *4LB* model, the tetrameric β-barrel-like pore is intrinsically-sealed in the central half of the pore, in the *8IB* model the pore is sealed by interlocking β1β2 loops from neighboring tetramers. Consequently, the two models differ (i) in the interface joining the neighboring tetramers and (ii) in the pore-lining close to the pore center. Thus, the interaction mode is relevant for the assembly of TJ-strands and for specifying the electrostatic properties and the shape of the pore center. The data presented here suggest these channel and strand characteristics to be defined according to the *8IB* model. This is of high relevance for determination of homo- and hetero-compatibility of different claudins [5,16,57], as

well as for analysis of the ion permeability of claudin channels. While one ion permeability study was based on a *8IB*-like dodecamer [25], others restricted the analysis to a tetramer and did not consider the influence of the interlocked chains [21,22,27,53]. While the latter studies importantly established a fundament for the analysis of the energetics of ion selectivity of claudin channels, future investigations might benefit from consideration of bigger oligomers.

Furthermore, the *8IB* model was used to investigate the mechanism causing the different preference for monovalent cations and water permeability of CLDN10b (Eisenman Sequence X/XI), (largely) water impermeable) and −15 (Eisenman Sequence I-IV, water permeable) [33,49,51]. The simulations of CLDN10b_wt, CLDN10b_K64M and CLDN15-like CLDN10b_D36H/A47E/A52S/Y45I/K64W/E153G indicated that the positive charge of the CLDN10b-specifc K64 competes with Na$^+$ for interaction with the central D56 cluster, whereas the CLDN10b-specific D36 and E153 increase the interaction and thus the attraction and density of Na$^+$ in the pore. Consequently, these results suggest that the charge distribution along the pore – differing between CLDN10b and -15 – affects guidance of the ions through the channels (Fig. 10, Fig. S3). We propose that this contributes critically to the different ion dehydration capacity (Eisenman Sequence) and water permeability of CLDN10b and -15 channels. In particular, for CLDN10b, the high density of negatively charged residues could cause a high Na$^+$-density along the pore. The presence of the flexibly oriented K64 between D56 and D36 could slow down the Na$^+$ flow across the pore center. In sum, the cation jamming may prevent efficient water permeation. Thus, dissimilar to CLDN2 but similar to CLDN15 channels [49], water would compete with cations for permeation in CLDN10b channels. Though, for CLDN10b channels water is much stronger disfavored than for CLDN15 channels. The biophysical analysis of model-derived mutants expressed in model cell lines [33,49] will be used in future studies to verify this concept.

Thus, the models provide novel insights into the mechanisms of regulation of paracellular ion and water permeability by the CLDN10b/-15 subgroup of claudins. This regulation is of relevance for the ion and water transport across epithelia in many organs, such as the kidney, intestine and exocrine glands [11].

5. Conclusions

MD simulations of double-membrane-embedded CLDN10b dodecamers suggest a joined double rows arrangement with *octameric-interlocked* pore barrels for this tight junction protein leading to paracellular cation channels. Adjacent, sidewise-unsealed tetrameric pore scaffolds are interlocked via the ECS1-β1β2 loop. On the one hand, this loop mediates hydrophobic clustering between chains of adjacent tetrameric pore scaffolds. On the other hand, it contributes to lining of the ion conduction pathway. This oligomerization mechanism is proposed to be conserved among classic claudins. However, the charge-distribution along the pore differing between CLDN10b and -15 is suggested to be a key determinant for the cation- and water permeabilities that differ between the two claudins.

CRediT authorship contribution statement

Santhosh Kumar Nagarajan: Investigation, Formal analysis, Visualization, Methodology, Writing – review & editing. **Stanislav Klein:** Investigation, Formal analysis, Visualization, Methodology. **Bita Sokhandan Fadakar:** Formal analysis, Methodology, Writing – review & editing. **Jörg Piontek:** Conceptualization, Supervision, Investigation, Formal analysis, Visualization, Writing – original draft, Writing – review & editing.

Declaration of Competing Interest

The authors declare that they have no known competing financial interests or personal relationships that could have appeared to influence the work reported in this paper.

Acknowledgements

Appendix A. Supporting information

Supplementary data associated with this article can be found in the online version at doi:10.1016/j.csbj.2023.02.009.

References

[1] Farquhar MG, Palade GE. Junctional complexes in various epithelia. J Cell Biol 1963;17:375–412.

[2] Staehelin LA, Mukherjee TM, Williams AW. Fine structure of frozen-etched tight junctions. Naturwissenschaften 1969;56:142.

[3] Staehelin LA, Mukherjee TM, Williams AW. Freeze-etch appearance of the tight junctions in the epithelium of small and large intestine of mice. Protoplasma 1969;67:165–84.

[4] Kaufmann R, Piontek J, Grull F, Kirchgessner M, Rossa J, Wolburg H, et al. Visualization and quantitative analysis of reconstituted tight junctions using localization microscopy. PLos One 2012;7:e31128.

[5] Gonschior H, Schmied C, Van der Veen RE, Eichhorst J, Himmerkus N, Piontek J, et al. Nanoscale segregation of channel and barrier claudins enables paracellular ion flux. Nat Commun 2022;13:4985.

[6] Zihni C, Mills C, Matter K, Balda MS. Tight junctions: from simple barriers to multifunctional molecular gates. Nat Rev Mol Cell Biol 2016;17:564–80.

[7] Beutel O, Maraspini R, Pombo-Garcia K, Martin-Lemaitre C, Honigmann A. Phase separation of zonula occludens proteins drives formation of tight junctions. Cell 2019;179. 923-936.e911.

[8] Rouaud F, Sluysmans S, Flinois A, Shah J, Vasileva E, Citi S. Scaffolding proteins of vertebrate apical junctions: structure, functions and biophysics. Biochim Et Biophys Acta Biomembr 2020;1862:183399.

[9] Otani T, Nguyen TP, Tokuda S, Sugihara K, Sugawara T, Furuse K, et al. Claudins and JAM-A coordinately regulate tight junction formation and epithelial polarity. J Cell Biol 2019;218:3372–96.

[10] Piontek J, Krug SM, Protze J, Krause G, Fromm M. Molecular architecture and assembly of the tight junction backbone. Biochim Et Biophys Acta Biomembr 2020;1862:183279.

[11] Gunzel D, Fromm M. Claudins and other tight junction proteins. Compr Physiol 2012;2:1819–52.

[12] Krause G, Winkler L, Mueller SL, Haseloff RF, Piontek J, Blasig IE. Structure and function of claudins. Biochim Biophys Acta 2008;1778:631–45.

[13] Piontek J, Winkler L, Wolburg H, Müller SL, Zuleger N, Piehl C, et al. Formation of tight junction: determinants of homophilic interaction between classic claudins. FASEB J: Publ Fed Am Soc Exp Biol 2008;22:146–58.

[14] Suzuki H, Tani K, Tamura A, Tsukita S, Fujiyoshi Y. Model for the architecture of claudin-based paracellular ion channels through tight junctions. J Mol Biol 2015;427:291–7.

[15] Hempel C, Protze J, Altun E, Riebe B, Piontek A, Fromm A, et al. Assembly of tight junction strands: claudin-10b and claudin-3 form homo-tetrameric building blocks that polymerise in a channel-independent manner. J Mol Biol 2020;432:2405–27.

[16] Daugherty BL, Ward C, Smith T, Ritzenthaler JD, Koval M. Regulation of heterotypic claudin compatibility. J Biol Chem 2007;282:30005–13.

[17] Milatz S, Himmerkus N, Wulfmeyer VC, Drewell H, Mutig K, Hou J, et al. Mosaic expression of claudins in thick ascending limbs of Henle results in spatial separation of paracellular Na+ and Mg2+ transport. Proc Natl Acad Sci USA 2017;114:E219–27.

[18] Irudayanathan FJ, Wang N, Wang X, Nangia S. Architecture of the paracellular channels formed by claudins of the blood-brain barrier tight junctions. Ann N Y Acad Sci 2017;1405:131–46.

[19] Zhao J, Krystofiak ES, Ballesteros A, Cui R, Van Itallie CM, Anderson JM, et al. Multiple claudin-claudin cis interfaces are required for tight junction strand formation and inherent flexibility. Commun Biol 2018;1:50.

[20] Rajagopal N, Nangia S. Unique structural features of claudin-5 and claudin-15 lead to functionally distinct tight junction strand architecture. Ann N Y Acad Sci 2022;1517:225–33.

[21] Berselli A, Alberini G, Benfenati F, Maragliano L. Computational study of ion permeation through claudin-4 paracellular channels. Ann N Y Acad Sci 2022;1516:162–74.

[22] Berselli A, Alberini G, Benfenati F, Maragliano L. Computational assessment of different structural models for claudin-5 complexes in blood-brain barrier tight junctions. ACS Chem Neurosci 2022;13:2140–53.

[23] Berselli A, Benfenati F, Maragliano L, Alberini G. Multiscale modelling of claudin-based assemblies: a magnifying glass for novel structures of biological interfaces. Comput Struct Biotechnol J 2022;20:5984–6010.

[24] Alberini G, Benfenati F, Maragliano L. A refined model of claudin-15 tight junction paracellular architecture by molecular dynamics simulations. PLoS One 2017;12:e0184190.

[25] Samanta P, Wang Y, Fuladi S, Zou J, Li Y, Shen L, et al. Molecular determination of claudin-15 organization and channel selectivity. J Gen Physiol 2018;150:949–68.

[26] Milatz S, Piontek J, Schulzke JD, Blasig IE, Fromm M, Gunzel D. Probing the cis-arrangement of prototype tight junction proteins claudin-1 and claudin-3. Biochem J 2015;468:449–58.

[27] Alberini G, Benfenati F, Maragliano L. Molecular dynamics simulations of ion selectivity in a claudin-15 paracellular channel. J Phys Chem B 2018;122:10783–92.

[28] Fuladi S, McGuinness S, Shen L, Weber CR, Khalili-Araghi F. Molecular mechanism of claudin-15 strand flexibility: a computational study. J Gen Physiol 2022;154. e202213116.

[29] Suzuki H, Nishizawa T, Tani K, Yamazaki Y, Tamura A, Ishitani R, et al. Crystal structure of a claudin provides insight into the architecture of tight junctions. Sci (N Y, N Y) 2014;344:304–7.

[30] Janson G, Paiardini A. PyMod 3: a complete suite for structural bioinformatics in PyMOL. Bioinformatics 2020;37:1471–2.

[31] Jumper J, Evans R, Pritzel A, Green T, Figurnov M, Ronneberger O, et al. Highly accurate protein structure prediction with AlphaFold. Nature 2021;596:583–9.

[32] Evans R, O'Neill M, Pritzel A, Antropova N, Senior A, Green T, et al. Protein complex prediction with AlphaFold-Multimer. bioRxiv 2022. 2021.2010.2004.463034.

[33] Hempel C, Rosenthal R, Fromm A, Krug SM, Fromm M, Gunzel D, et al. Tight junction channels claudin-10b and claudin-15: functional mapping of pore-lining residues. Ann N Y Acad Sci 2022;1515:129–42.

[34] Bowers, K.J. , Chow, E. , Xu, H. , Dror, R.O. , Eastwood, M.P. , Gregersen, B.A. , , , , , , , , and et al. (2006) Scalable Algorithms for Molecular Dynamics Simulations on Commodity Clusters. ACM/IEEE SC 2006 Conference (SC'06), 43–43.

[35] Lomize MA, Pogozheva ID, Joo H, Mosberg HI, Lomize AL. OPM database and PPM web server: resources for positioning of proteins in membranes. Nucleic Acids Res 2012;40. D370-376.

[36] Jorgensen WL, Chandrasekhar J, Madura JD, Impey RW, Klein ML. Comparison of simple potential functions for simulating liquid water. J Chem Phys 1983;79:926–35.

[37] Roos K, Wu C, Damm W, Reboul M, Stevenson JM, Lu C, et al. OPLS3e: extending force field coverage for drug-like small molecules. J Chem Theory Comput 2019;15:1863–74.

[38] Kurki M, Poso A, Bartos P, Miettinen MS. Structure of POPC lipid bilayers in OPLS3e force field. J Chem Inf Model 2022.

[39] Martyna GJ, Klein ML, Tuckerman ME. Nosé-Hoover chains: the canonical ensemble via continuous dynamics. J Chem Phys 1992;97:2635–43.

[40] Martyna GJ, Tobias DJ, Klein ML. Constant pressure molecular dynamics algorithms. J Chem Phys 1994;101:4177–89.

[41] Nakamura S, Irie K, Tanaka H, Nishikawa K, Suzuki H, Saitoh Y, et al. Morphologic determinant of tight junctions revealed by claudin-3 structures. Nat Commun 2019;10:816.

[42] Rossum, G. v, and Drake, F.L. (2009) Python 3 Reference Manual.

[43] Michaud-Agrawal N, Denning EJ, Woolf TB, Beckstein O. MDAnalysis: a toolkit for the analysis of molecular dynamics simulations. J Comput Chem 2011;32:2319–27.

[44] Gowers, R.J. , Linke, M. , Barnoud, J. , Reddy, T. , Melo, M.N. , Seyler, S.L. , , , , , and et al. (2016) MDAnalysis: A Python Package for the Rapid Analysis of Molecular Dynamics Simulations. Proceedings of the 15th Python in Science Conference, 98–105.

[45] Smart OS, Goodfellow JM, Wallace BA. The pore dimensions of gramicidin A. Biophys J 1993;65:2455–60.

[46] Smart OS, Neduvelil JG, Wang X, Wallace BA, Sansom MS. HOLE: a program for the analysis of the pore dimensions of ion channel structural models. J Mol Graph 1996;14:354–60. 376.

[47] McGibbon RT, Beauchamp KA, Harrigan MP, Klein C, Swails JM, Hernandez CX, et al. MDTraj: a modern open library for the analysis of molecular dynamics trajectories. Biophys J 2015;109:1528–32.

[48] Kabsch W, Sander C. Dictionary of protein secondary structure: pattern recognition of hydrogen-bonded and geometrical features. Biopolymers 1983;22:2577–637.

[49] Rosenthal R, Gunzel D, Piontek J, Krug SM, Ayala-Torres C, Hempel C, et al. Claudin-15 forms a water channel through the tight junction with distinct function compared to claudin-2. Acta Physiol 2020;228:e13334.

[50] Colegio OR, Van Itallie CM, McCrea HJ, Rahner C, Anderson JM. Claudins create charge-selective channels in the paracellular pathway between epithelial cells. Am J Physiol Cell Physiol 2002;283:142–7.

[51] Günzel D, Stuiver M, Kausalya PJ, Haisch L, Krug SM, Rosenthal R, et al. Claudin-10 exists in six alternatively spliced isoforms that exhibit distinct localization and function. J Cell Sci 2009;122:1507–17.

[52] Rosenthal R, Milatz S, Krug SM, Oelrich B, Schulzke JD, Amasheh S, et al. Claudin-2, a component of the tight junction, forms a paracellular water channel. J Cell Sci 2010;123:1913–21.

[53] Irudayanathan FJ, Wang X, Wang N, Willsey SR, Seddon IA, Nangia S. Self-assembly simulations of classic claudins-insights into the pore structure, selectivity, and higher order complexes. J Phys Chem B 2018;122:7463–74.

[54] Nusrat A, Parkos CA, Verkade P, Foley CS, Liang TW, Innis-Whitehouse W, et al. Tight junctions are membrane microdomains. J Cell Sci 2000;113(Pt 10):1771–81.

[55] Kady NM, Liu X, Lydic TA, Syed MH, Navitskaya S, Wang Q, et al. ELOVL4-mediated production of very long-chain ceramides stabilizes tight junctions and prevents. Diabetes-Induc Retin Vasc Permeab *Diabetes* 2018;67:769–81.

[56] Van Itallie CM, Rogan S, Yu A, Vidal LS, Holmes J, Anderson JM. Two splice variants of claudin-10 in the kidney create paracellular pores with different ion selectivities. Am J Physiol Ren Physiol 2006;291. F1288-F1299.

[57] Piontek J, Fritzsche S, Cording J, Richter S, Hartwig J, Walter M, et al. Elucidating the principles of the molecular organization of heteropolymeric tight junction strands. Cell Mol Life Sci:CMLS 2011;68:3903–18.